Incremental pressure correction method for high-performance simulations of subsonic compressible flows

Jerome Jansen[a,b], Stéphane Glockner[a,b,*], Deewakar Sharma[a,b], Arnaud Erriguible[a,b,c]

[a] *Univ. Bordeaux CNRS, Bordeaux INP, I2M, UMR 5295, F-33400, Talence, France*
[b] *Arts et Metiers Institute of Technology, CNRS, Bordeaux INP, Hesam Universite, I2M, UMR 5295 , F-33400, Talence, France*
[c] *Univ. Bordeaux, CNRS, Bordeaux INP, ICMCB, UMR 5026 , F-33600, Pessac, France*

Abstract

In the present work, we propose a time-splitting method to handle the treatment of pressure-velocity coupling in the context of subsonic compressible flows. We extend the well-known *incremental pressure correction method for incompressible flows* to subsonic compressible flows by solving an Helmholtz-type equation for the temporal pressure increment variable. The governing equations, written in primitive variables, consist of the compressible Navier–Stokes equations along with the energy conservation equation. Closure with any chosen fluid equation of state enables the calculation of relevant thermophysical fluid properties. After deriving the proposed method and recalling its *non-incremental* counterpart, spatial and temporal second-order convergence are measured for both methods on various verification test cases. The classical pressure accuracy limitations of the *non-incremental* method for incompressible flows are overcome when applied to compressible subsonic flows due to the different nature of the pressure equation. The *incremental* method is subsequently applied to steady and unsteady high-gradient temperature and density flows, *i.e.* beyond the Boussinesq approximation known as Non-Oberbeck-Boussinesq flows, such as thermoacoustic wave propagation and natural convection problems. Both verification and validation processes are systematically and carefully detailed. Finally, Direct Numerical Simulation of three-dimensional compressible Rayleigh–Bénard turbulent convection of highly compressible fluid supercritical carbon dioxide is proposed. The parallel implementation efficiency of the method is also reported throught strong and weak scalability tests in the last three-dimensional case up to 131,072 cores. We demonstrate the capacity to provide a full second-order accurate and efficient incremental pressure correction method to solve subsonic compressible flows.

Keywords: subsonic compressible flows, time-splitting, incremental pressure correction method, natural convection, thermoacoustic wave, Rayleigh–Bénard, Non-Oberbeck-Boussinesq

Code availability. The implementation of the proposed method and all the presented test cases are available in the Notus CFD Git repository https://git.notus-cfd.org/ (code v0.6.0) which significantly enhances the reproducibility of the present work.

*Corresponding author.
Email addresses: jerome.jansen@u-bordeaux.fr (Jerome Jansen), stephane.glockner@bordeaux-inp.fr (Stéphane Glockner), deewakar.edu@gmail.com (Deewakar Sharma), arnaud.erriguible@bordeaux-inp (Arnaud Erriguible)

Contents

1. Introduction

The current climate situation necessitates the development of innovative strategies to meet the future energy demands through sustainable energy processes simultaneously addressing the climate crisis. In the recent years, several solutions have been proposed in both energy production and energy storage. Among others, we can cite hydrogen storage and production, carbon dioxide storage, carbon dioxide plume gas technology using subsurface CO_2 for power generation, trans-critical CO_2 power cycle for efficient power generation. In such processes, working fluids are submitted to high pressure and/or high temperature and become highly compressible and at subsonic regime. It is thereby evident that for advancing the sustainable energy processes enhancement, both from scientific as well as technological perspectives, comprehending the fluid behaviour in high pressure (and temperature) systems is of prime importance. This perspective creates an imminent need to develop modelling and simulating tools which could provide insights into the flow dynamics varying from local scale to real applications scales. This need converges with advancements in hardware architectures and the rise of large-scale computational clusters, which have ushered in a paradigm shift in computational science. Petascale supercomputers, capable of running simulations on more than 100,000 processors, are now increasingly common. While this computational power offers unprecedented opportunities, it also introduces significant challenges at every level of a Computational Fluid Dynamics code, including numerical methods, I/O, visualization. Although currently limited to specialized teams and codes, such capabilities are expected to become widespread in the near future, creating a pressing need for codes that are not only robust and general, but also easy to use and adaptable to evolving architectures.

In CFD codes, solving pressure equations - an essential component intricately linked to velocity-pressure coupling - remains one of the most computationally expensive aspects of simulations. Reducing CPU time and maximizing parallel efficiency are therefore critical to fully harness the power of modern supercomputing resources. Moreover, addressing pressure-velocity coupling for both incompressible and compressible fluid problems constitutes a rich and complex research domain. State-of-the-art methods face several key challenges that must be addressed to ensure their applicability and robustness for high-fidelity simulations. These challenges include achieving high spatial and temporal convergence orders, managing significant fluid properties variations, enhancing numerical stability, and implementing robust outflow boundary conditions.

The common classification for solving compressible flow problems divides methods into density-based and pressure-based. Both methods use the momentum equation to calculate velocity field and primarily differ in their approach to calculate the density and the pressure fields. Coming from the supersonic flow community [1, 2, 3], density-based methods access the density by solving the mass conservation equation and use the equation of state for computing the pressure field. Though the method has been mainly designed for high Mach flows, several authors [4, 5] have extended its utility to Mach number less than 0.3 problems by addressing the inaccuracy arising in this limit case. Pressure-based methods, initially developed within the incompressible flow community [6, 7] have been extended to low-Mach or weakly compressible flows [8, 9, 10, 11, 12, 13, 14] and all-speed flows [15, 16, 17, 18]. They are characterized by solving implicitly a derived pressure equation from a combination of momentum, mass (and energy) conservation. The density field can be computed from an equation of state knowing the resolved pressure field. The proposed method in this article belongs to the pressure-based category of methods.

For incompressible flows, the often referred "pressure correction methods" or "fractional step methods" are widely employed. These methods involve initially predicting the velocity field by solving the conservation of momentum equation, followed by one or more correction steps to obtain the pressure and a solenoidal velocity field. Within this family of methods, the present work focuses on non-iterative projection methods, and does not consider any iteration or update for the computation of the pressure variable. Approaches like the PISO or SIMPLE algorithms [7, 19, 14], which require several iterations for SIMPLE and updates for PISO on a pressure correction variable to achieve the divergence-free constraint, are beyond the scope of this study. A pioneering projection method, still widely used, was developed by Chorin [6]. It involves solving the prediction step by neglecting the pressure gradient in the momentum equation, followed by solving a Laplacian on the pressure, with the gradient used to ensure a divergence-free velocity field. While applicable to both single-phase and two-phase flows, this method is known to suffer from a low temporal convergence order. The Chorin method was later improved upon by Goda [20] and subsequently by Timmermans et al. [21], introducing the *incremental pressure correction method* and the *rotational incremental pressure correction method*, respectively.

Unlike Chorin's method, labelled *non-incremental pressure correction method*, both Goda's and Timmermans' methods incorporate the pressure gradient in the prediction stage. The unknown resolved variable in the correction stage is the temporal increment of the pressure. The precise mathematical analysis of these schemes has been carried out in the work of Guermond et al. [22]. An important parameter to characterize a resolution methodology is the order of convergence, both in space and time. In the aforementioned methods of Chorin [6] and Goda [20], the boundary condition on the pressure or its increment creates an artificial boundary layer that does not compromise the spatial precision of the discretization. However, there are significant differences in the order of temporal convergence among the original method and its variants. According to Guermond et al. [22], with Dirichlet boundary conditions applied on the velocity, the standard non-incremental method by Chorin [6] converges in time at order 1 for velocity and 1/2 for pressure. In comparison, the incremental standard method by Goda [20] converges at orders 2 and 1 for velocity and pressure, respectively, while the incremental rotational method by Timmermans et al. [21] — reducing the artificial boundary layer — converges at orders 2 and 3/2 for velocity and pressure, respectively.

In the context of compressible subsonic flows and pressure-based projection methods, the full form of the mass conservation equation and thermodynamic effects make the resolution of the pressure-velocity coupling even more complex. For more than two decades, several authors have proposed methods based on an Helmholtz-type equation for the pressure [23, 17, 24, 18, 12, 25, 26, 27] that can be considered as *non-incremental pressure correction methods* for compressible flows. They have been successfully applied to single as well as multiphase flows. The study that comes closest to the method proposed in this paper was conducted by Reichling et al. [28]. Their method belongs to the *incremental pressure correction method* category as it solves a pressure increment variable by solving an elliptic equation with variable coefficients plus a three steps velocity calculation. Their algorithm considers perfect gas equation of state and the governing equations are written in a conservative form with the need to evaluate the divergence of the momentum. They achieve a second-order time accuracy on the linear acoustic test case. To the best of the authors' knowledge, the incremental pressure correction method written in primitive variables for any fluid equation of state has not yet been proposed.

Further, though some works can be found where the authors have performed spatial convergence studies for compressible flows using manufactured or exact solutions [9, 29, 24, 30, 31, 14], very few have presented temporal convergence studies [9, 27, 28, 13, 14]. Among the limited work to the author's knowledge, Moureau et al. [27], Reichling et al. [28], and Cang and Wang [14] conduct a temporal convergence study on the linear acoustic propagation problem with periodic boundary conditions, demonstrating a second-order temporal accuracy for the first two and first-order for the latter. Considering a pressure-based discontinuous Galerkin method, Hennink et al. [13] proposed a general manufactured solution of the compressible Navier-Stokes equation coupled with enthalpy equation. On constant- and variable-density solutions with Dirichlet and Neumann boundary conditions, they observed full second-order temporal accuracy. To the best of the authors' knowledge, no systematic evaluation of the accuracy and order of convergence of *non-* and *incremental correction methods* for compressible subsonic flows has been proposed in the literature.

This article presents the Incremental Pressure Correction Method, written in primitive variable, for general Subsonic compressible Flows (IPCMSF). While for incompressible flows, the traditional approach for constructing the correction step in this class of methods relies on the null divergence property of the velocity field, our method for compressible flows involves leveraging the pressure equation [32], which includes a divergence term of the velocity. Furthermore, IPCMSF couples the Navier-Stokes equation with the energy conservation equation written in temperature variable and with any chosen equation of state for the calculation of material properties, including the density. The key feature of this work has been to achieve second-order spatial and temporal accuracy, for velocity, pressure, temperature and density for both incremental and *non*-incremental pressure correction methods, IPCMSF and PCMSF, respectively. The verification process, systematically and carefully detailed, presents temporal convergence studies for different benchmarks of increasing complexity, from 0D test case to manufactured 2D solution with variable thermophysical properties and Dirichlet boundary conditions for velocity and temperature. The validation process is also carefully detailed and covers stationary to unsteady thermally driven flows (free convection and thermoacoustic wave propagation). Both the validation and verification processes provide a carefully addressed, extensive database of test cases to support further development within the CFD community. Finally, in order to project the proposed method towards future challenges related to high pressure and/or high temperature flows, a large

numerical experiment of a 3D turbulent Rayleigh-Bénard flow, as well as high-performance computing considerations, are discussed. The current work focuses only on single-phase highly compressible flow with Dirichlet boundary conditions on velocity, while outlet/open boundary conditions and considerations for multiphase flow are beyond the scope of this article and will be covered up in future works.

The article is structured as follows: Section 2 presents a review of the governing equations for compressible flow in primitive variables; In Section 3, we propose the pressure increment correction method applied to subsonic compressible flows; Section 4 focuses on the numerical framework, employing implicit discretization of the equations using the second-order finite volume method with first and second-order temporal orders; Section 5 illustrates various test cases for verification of the developed method covering (a) isentropic injection and linear acoustic pulse propagation test cases and (b) a manufactured solution tailored to low to Mach numbers close to 0.6. These cases are utilized to compute spatial and temporal convergence orders; Section 6 presents steady and unsteady 2D natural convection test cases, outside the Boussinesq approximation known as Non-Oberbeck-Boussinesq effects, focusing on various ranges of subsonic Mach numbers. Thermoacoustic wave propagation in perfect gas and supercritical carbon dioxide are also studied; Section 7.1 presents an application of IPCMSF to conduct a turbulent Rayleigh–Bénard Direct Numerical Simulation of supercritical carbon dioxide. The last Section 7.2 discusses the parallel efficiency of the IPCMSF implementation, through both strong and weak scalability tests on the three-dimensional configuration presented in Section 7.1. Lastly, conclusions and perspectives are provided in Section 8.

2. Governing equations

2.1. Classical formulation of a compressible flow

Under the Newtonian fluid hypothesis, the governing equations of a compressible flow expresses the conservation of mass, momentum, energy in c_p formulation, respectively

$$\frac{\partial \rho}{\partial t} + \boldsymbol{v} \cdot \boldsymbol{\nabla} \rho = -\rho \boldsymbol{\nabla} \cdot \boldsymbol{v} \,, \tag{1a}$$

$$\rho \left(\frac{\partial \boldsymbol{v}}{\partial t} + (\boldsymbol{v} \cdot \boldsymbol{\nabla}) \, \boldsymbol{v} \right) = -\boldsymbol{\nabla} p + \boldsymbol{\nabla} \cdot (\mu \dot{\boldsymbol{\gamma}}) - \frac{2}{3} \boldsymbol{\nabla} \left(\mu \boldsymbol{\nabla} \cdot \boldsymbol{v} \right) + \rho \boldsymbol{g} \,, \tag{1b}$$

$$\rho c_p \left(\frac{\partial T}{\partial t} + \boldsymbol{v} \cdot \boldsymbol{\nabla} T \right) = T \beta_p \left(\frac{\partial p}{\partial t} + \boldsymbol{v} \cdot \boldsymbol{\nabla} p \right) + \boldsymbol{\nabla} \cdot (\lambda \boldsymbol{\nabla} T) + \Phi_d \,. \tag{1c}$$

We add to this classical formulation a derived pressure-energy equation

$$\frac{\partial p}{\partial t} + \boldsymbol{v} \cdot \boldsymbol{\nabla} p = -\rho c^2 \boldsymbol{\nabla} \cdot \boldsymbol{v} + \frac{\beta_p c^2}{c_p} \left(\boldsymbol{\nabla} \cdot (\lambda \boldsymbol{\nabla} T) + \Phi_d \right) \,. \tag{2}$$

A descriptive derivation of pressure-energy equation is provided in Appendix A.

These conservation equations are written in terms of primitive variables, with $T(\boldsymbol{x}, t)$ the temperature field, $p(\boldsymbol{x}, t)$ the pressure field, $\boldsymbol{v}(\boldsymbol{x}, t)$ the velocity field, and $\rho(\boldsymbol{x}, t)$ the density field. In (1b), the strain rate tensor is defined as $\dot{\boldsymbol{\gamma}} = \boldsymbol{\nabla} \boldsymbol{v} + \boldsymbol{\nabla} \boldsymbol{v}^T$, μ is the dynamic viscosity of the fluid, $\boldsymbol{g}$ is the gravitational acceleration, and we consider the Stokes' hypothesis for the second coefficient of viscosity $\lambda_\mu = -2\mu/3$. In equations (1c) and (2), c_p denotes the specific heat capacity, $\beta_p = -\rho^{-1} \left(\partial \rho / \partial T \right)_p$ is the isobaric thermal expansion coefficient, λ is the thermal conductivity, and Φ_d is the viscous dissipation rate of energy defined as

$$\Phi_d = -\frac{2\mu}{3} \left(\boldsymbol{\nabla} \cdot \boldsymbol{v} \right)^2 + \frac{\mu}{2} \dot{\boldsymbol{\gamma}} : \dot{\boldsymbol{\gamma}} \,. \tag{3}$$

For the sake of generalization, we have introduced Φ_d within the equations of the article, but this term will be ignored in all the simulations in Sections 5 and 6.

To close the system of equations introduced above and preventing the problem to be ill-posed, in addition to specifying the initial and boundary conditions, an equation of state (EoS) for the density and other material properties x, *e.g.* isothermal compressibility, thermal expansion, speed of sound or heat capacity must be chosen as

$$x = \mathrm{EoS}(T, p) \,. \tag{4}$$

While several authors have already used the introduced modelling with equations (1) along with the pressure-energy equation (2) [15, 33, 27, 23, 34, 35, 36, 32, 12, 25, 37], the originality of the proposed approach is to use (2) to derive the IPCMSF. In addition, the proposed modelling of a compressible flow (1) (4) as well as our method as presented in Section 3 make no assumptions about the type of fluid thereby making it feasible to cover a wide range of fluids using any appropriate EoS.

3. The incremental pressure correction method

3.1. Derivation of the equation for the pressure increment variable

An incremental pressure correction approach for compressible flow requires the development and the resolution of an equation specifically dedicated to the temporal pressure increment, denoted by φ. Following the original incremental pressure correction method applied for incompressible flows [20], we write the pressure at next iteration as $p^{n+1}=p^n+\varphi$.

Since density varies in compressible flows, the first step of the current method seeks to have an estimate of the density field, ρ^{n+1}, denoted by $\rho^\dagger$. This is obtained through extrapolation at the desired order, *e.g.* for first-order in time $\rho^\dagger=\rho^n$ and for second-order in time with constant time step as $\rho^\dagger=2\rho^n-\rho^{n-1}$. Henceforth, any variable $x^\dagger$ will be an estimate of x at the order of the chosen temporal scheme.

A predicted velocity, denoted by $\boldsymbol{v}^*$, is obtained by solving the momentum equation considering the pressure gradient at time t^n

$$\rho^\dagger\left(\frac{a\boldsymbol{v}^*+b\boldsymbol{v}^n+c\boldsymbol{v}^{n-1}}{\Delta t}+\boldsymbol{\nabla}\cdot(\boldsymbol{v}^\dagger\otimes\boldsymbol{v}^*)-\boldsymbol{v}^*\boldsymbol{\nabla}\cdot\boldsymbol{v}^\dagger\right)=-\boldsymbol{\nabla}p^n+\boldsymbol{\nabla}\cdot\left(\mu^\dagger\dot{\boldsymbol{\gamma}}^*\right)-\frac{2}{3}\boldsymbol{\nabla}\left(\mu^\dagger\boldsymbol{\nabla}\cdot\boldsymbol{v}^*\right)+\rho^\dagger\boldsymbol{g}\,, \tag{5}$$

with a,b,c denoting the time discretization coefficients of first-order Euler backward scheme ($a=1$, $b=-1$, $c=0$) or second-order Backward Differentiation Formula ($a=3/2$, $b=-2$, $c=1/2$). Equation (5) is written in its fully implicit form, but it could also be written in semi- or fully-explicit form depending on the scales of a given problem.

Following Goda's classical approach, we write the pressure increment equation by taking the difference between (1b) evaluated at time t^{n+1} and (5), while neglecting the nonlinear and the divergence terms of the stress tensor, as

$$\boldsymbol{v}^{n+1}-\boldsymbol{v}^*=-k_\varphi^\dagger\boldsymbol{\nabla}\varphi\,, \tag{6}$$

with $k_\varphi^\dagger=\frac{\Delta t}{a\rho^\dagger}$. Taking the divergence of (6), it reads

$$\boldsymbol{\nabla}\cdot\boldsymbol{v}^{n+1}-\boldsymbol{\nabla}\cdot\boldsymbol{v}^*=-\boldsymbol{\nabla}\cdot\left(k_\varphi^\dagger\boldsymbol{\nabla}\varphi\right)\,. \tag{7}$$

Compared to incompressible flows, where we have a divergence-free velocity, we aim to replace the velocity divergence term in compressible flows $\boldsymbol{\nabla}\cdot\boldsymbol{v}^{n+1}$ in (7) by the following relation coming from the discretized pressure-energy equation (2)

$$\frac{ap^{n+1}+bp^n+cp^{n-1}}{\Delta t}+\boldsymbol{v}^\dagger\cdot\boldsymbol{\nabla}p^\dagger=-(\rho c^2)^\dagger\boldsymbol{\nabla}\cdot\boldsymbol{v}^{n+1}+\left(\frac{\beta_p c^2}{c_p}\right)^\dagger\left(\boldsymbol{\nabla}\cdot(\lambda^\dagger\boldsymbol{\nabla}T^\dagger)+\Phi_d^\dagger\right)\,. \tag{8}$$

By rearranging the terms and by expressing φ, we obtain

$$\boldsymbol{\nabla}\cdot\boldsymbol{v}^{n+1}=\left(-\frac{a\varphi}{\Delta t}-\frac{(a+b)p^n+cp^{n-1}}{\Delta t}-\boldsymbol{v}^\dagger\cdot\boldsymbol{\nabla}p^\dagger+\left(\frac{\beta_p c^2}{c_p}\right)^\dagger\left(\boldsymbol{\nabla}\cdot(\lambda^\dagger\boldsymbol{\nabla}T^\dagger)+\Phi_d^\dagger\right)\right)\Big/(\rho c^2)^\dagger\,. \tag{9}$$

Finally, combining (9) and (7), we obtain the following Helmholtz-type equation with variable coefficients for the pressure increment

$$\frac{a\varphi}{(\rho c^2)^\dagger\Delta t}-\boldsymbol{\nabla}\cdot\left(k_\varphi^\dagger\boldsymbol{\nabla}\varphi\right)=-\boldsymbol{\nabla}\cdot\boldsymbol{v}^*+\frac{\dot{S}_\varphi^\dagger}{(\rho c^2)^\dagger}\,, \tag{10}$$

with the compressible pressure increment source term given by

$$\dot{S}^{\dagger}_{\varphi} = \left(\frac{\beta_p c^2}{c_p}\right)^{\dagger} \left(\boldsymbol{\nabla}\cdot(\lambda^{\dagger}\boldsymbol{\nabla}T^{\dagger}) + \Phi^{\dagger}_{d}\right) - \boldsymbol{v}^{\dagger}\cdot\boldsymbol{\nabla}p^{\dagger} - \frac{(a+b)p^n + cp^{n-1}}{\Delta t} \tag{11}$$

The derivation of the pressure equation for the *non-incremental pressure correction method* follows the same steps as described above but, without considering the pressure gradient $\boldsymbol{\nabla}p^n$ in (5) and solving the pressure variable p instead of φ in (10).

It is worth highlighting that within the incompressible limit case ($c\to\infty$ and $\beta_p=0$), the pressure increment equation (10) (or its counterpart pressure equation for *non-incremental* method) is reduced to that of the incompressible case. Thus, the proposed method is valid in the limit of incompressible flows. This has been numerically verified. As the results are strictly identical to those given by the *incremental pressure correction method* for incompressible flows, they are not discussed in the present work in order to better concentrate on various subsonic flows.

3.2. Full semi-implicit system of equation

This section sums up the proposed *incremental pressure correction method for compressible flow.*

Firstly, the material properties, as well as temperature field are extrapolated in time. Then, a predicted velocity is computed solving $\boldsymbol{v}^*$ as

$$\rho^{\dagger}\left(\frac{a\boldsymbol{v}^* + b\boldsymbol{v}^n + c\boldsymbol{v}^{n-1}}{\Delta t} + \boldsymbol{\nabla}\cdot(\boldsymbol{v}^{\dagger}\otimes\boldsymbol{v}^*) - \boldsymbol{v}^*\boldsymbol{\nabla}\cdot\boldsymbol{v}^{\dagger}\right) = -\boldsymbol{\nabla}p^n + \boldsymbol{\nabla}\cdot\left(\mu^{\dagger}\dot{\boldsymbol{\gamma}}^*\right) - \frac{2}{3}\boldsymbol{\nabla}\left(\mu^{\dagger}\boldsymbol{\nabla}\cdot\boldsymbol{v}^*\right) + \rho^{\dagger}\boldsymbol{g}\,, \tag{12}$$

with the generic non-homogeneous Dirichlet boundary condition $\boldsymbol{v^*}\cdot\boldsymbol{n}=\boldsymbol{v}\cdot\boldsymbol{n}$ at the boundary of the domain, denoted by Γ.

Then, the resolution of the pressure increment field is made by solving

$$\frac{a\varphi}{(\rho c^2)^{\dagger}\Delta t} - \boldsymbol{\nabla}\cdot\left(k^{\dagger}_{\varphi}\boldsymbol{\nabla}\varphi\right) = -\boldsymbol{\nabla}\cdot\boldsymbol{v}^* + \frac{\dot{S}^{\dagger}_{\varphi}}{(\rho c^2)^{\dagger}}\,, \tag{13}$$

with the homogeneous Neumann boundary condition $\partial\varphi/\partial n=0$ on Γ since the constraint $\boldsymbol{v^{n+1}}\cdot\boldsymbol{n}=\boldsymbol{v^*}\cdot\boldsymbol{n}$ is imposed in (6).

After solving φ, velocity and pressure are updated during a correction step as,

$$\boldsymbol{v}^{n+1} = \boldsymbol{v}^* - k^{\dagger}_{\varphi}\boldsymbol{\nabla}\varphi\,, \tag{14}$$

$$p^{n+1} = p^n + \varphi\,. \tag{15}$$

Once the velocity and pressure are corrected, the next step is to compute the corresponding temperature field using the (c_p, T) formulation of the energy conservation. The following is written in an implicit form

$$\begin{aligned}\rho^{\dagger}c^{\dagger}_{p}\left(\frac{aT^{n+1} + bT^n + cT^{n-1}}{\Delta t} + \left(\boldsymbol{\nabla}\cdot(\boldsymbol{v}T) - T\boldsymbol{\nabla}\cdot\boldsymbol{v}\right)^{n+1}\right) \\ - T^{n+1}\beta^{\dagger}_{p}\left(\frac{ap^{n+1} + bp^n + cp^{n-1}}{\Delta t} + \boldsymbol{v}^{n+1}\cdot\boldsymbol{\nabla}p^{n+1}\right) = \boldsymbol{\nabla}\cdot(\lambda^{\dagger}\boldsymbol{\nabla}T^{n+1}) + \Phi^{n+1}_{d}\,.\end{aligned} \tag{16}$$

Finally, we update the density, and the relevant thermophysical properties, of the fluid using an EoS just before moving to the next time iteration

$$x^{n+1} = \mathrm{EoS}(T^{n+1}, p^{n+1})\,. \tag{17}$$

The *non-incremental* counterpart can be obtained by (a) not taking into account the pressure gradient at the velocity prediction step (12); (b) considering the pressure instead of pressure increment variable; and (c) changing the compressible pressure increment source term $\dot{S}^{\dagger}_{\varphi}$ in (13) by a compressible pressure source term $\dot{S}^{\dagger}_{p}$ as

$$\dot{S}^{\dagger}_{p} = \left(\frac{\beta_p c^2}{c_p}\right)^{\dagger} \left(\boldsymbol{\nabla}\cdot(\lambda^{\dagger}\boldsymbol{\nabla}T^{\dagger}) + \Phi^{\dagger}_{d}\right) - \boldsymbol{v}^{\dagger}\cdot\boldsymbol{\nabla}p^{\dagger} - \frac{bp^n + cp^{n-1}}{\Delta t}\,. \tag{18}$$

3.3. Note on the expected pressure temporal convergence order for the non-incremental method

We recall that, under the incompressibility assumption with Dirichlet boundary conditions applied to the velocity, the standard non-incremental method by Chorin [6] converges in time at order 1 for velocity and order 1/2 for pressure [22]. For compressible flow, second-order convergence has been observed for the linear acoustic propagation problem with periodic boundary conditions [27, 28, 14]. However, there are no studies addressing the case of Dirichlet boundary conditions. A closer examination of the equation system for compressible flow offers insight into the expected temporal convergence order for pressure. Here, pressure is not merely a scalar field enforcing the incompressibility constraint; rather, it is a dynamic variable governed by its own temporal evolution equation (2). The divergence of velocity at time t^{n+1} is no longer zero but depends on the temporal derivative of pressure (9). This leads to equation (10) for pressure increment which includes a temporal variation term. Therefore, second-order temporal convergence is expected even with Dirichlet boundary conditions, and we do not anticipate, as observed for incompressible flows, significant differences in convergence for either method.

3.4. Note on the treatment of the volume penalization method

The immersed boundary of a solid can be treated by adding a volume penalization term $\chi\left(\boldsymbol{v}-\boldsymbol{v_0}\right)$ to the right-hand side of the momentum equation (1a) [38]. On a Cartesian grid and obstacles whose boundaries are parallel to the grid directions, a large value (10^{20}) of the parameter χ allows to assign the velocity $\boldsymbol{v}$ equal to the given velocity $\boldsymbol{v_0}$.

In such an approach, the incremental pressure correction method needs to be slightly corrected in order to maintain a Neumann boundary condition on the pressure increment at the immersed boundary. It can be easily shown that $k_\varphi^\dagger$ coefficient has to be replaced by

$$k_\varphi^\dagger = \frac{\Delta t}{a\rho^\dagger + \chi\Delta t}\,. \tag{19}$$

In a finite volume code, a large value of χ on the face of the cell at the boundary (geometrically interpolated from cell centre values) penalizes the pressure increment derivative to zero, effectively disconnecting the fluid and solid domains. This method converges spatially at first-order only and can be easily implemented by considering a Jacobi linear system preconditioning that locally reduces matrix coefficient to 1 instead of a value around 10^{20}.

4. Numerical methods

Both PCMSF and IPCMSF has been implemented within our in-house CFD code, named `Notus` [39], developed in Fortran 2008 under a free software licence. `Notus` employs the Finite Volume Method on a Cartesian staggered grid. In pursuit of computational efficiency and scalability, the code is designed for high-performance parallel computing up to petascale simulations [40].

For all the presented test cases in this article, an implicit second-order scheme is used for the advection terms, diffusion, and stress terms. BDF2 second-order time discretization is also employed, except when specifically mentioned for the first-order Euler scheme. The advected pressure gradient term of (11) is discretized with upwind second-order scheme and a decentering at boundaries of the domain to avoid boundary condition on pressure. Linear systems are solved using BiCGStab or GMRES Krylov iterative solvers, and geometric multigrid preconditioners (PFMG and SMG for regular and Chebychev grids, respectively) within the Hypre library [41]. The credibility and reliability of the code are established through a thorough verification, validation, and non-regression environment. `Notus` has been widely used in various scientific contexts [40, 42, 43, 44, 45, 46].

5. Verification

Verification and validation of a CFD code are essential steps in establishing a reliable numerical tool. These concepts are extensively discussed in [47] and [48], and are more broadly addressed in [49]. Verification is the process of determining whether the implementation of a model and its associated methods accurately represents its conceptual description and solution. The fundamental strategy of verification involves the identification, quantification, and reduction of errors in the numerical model

and its solution. Code verification encompasses solution verification on a set of problems for which the exact solution (available only for simplified problems) is known or manufactured. The latter does not necessarily require a connection with the reality of a physical phenomenon. Verification thus offers evidence that the continuous model is correctly solved by the discrete approach chosen in the calculation code. It is primarily a mathematical and computational process.

For each verification test case of this section, we present convergence studies of IPCMSF considering an analytical solution. Tables of the section present absolute euclidean norm $||\varepsilon_X||_{\mathrm{L}_2}$, infinity norm $||\varepsilon_X||_{\mathrm{L}_\infty}$ of the field X and the respective orders of convergence.

The comparison between IPCMSF and PCMSF is discussed in Section 5.4 in support of Appendix D in which we present the temporal convergence of the verification cases for the PCMSF.

5.1. Isentropic injection in a square cavity

As a first verification test case, we present the isentropic injection problem. A square cavity of length $L=1$ mm is filled with air considered as a perfect gas ($R=287$ J K^{-1} kg^{-1}, $\gamma=c_p/c_v=1.4$). At initial time, the following thermodynamic state is imposed $(T_0,p_0,\rho_0)=(300\mathrm{K},101325\mathrm{Pa},\frac{p_0}{RT_0})$. A fluid in the same thermodynamic state as the cavity is injected from the top with a vertical velocity $\boldsymbol{v}_{y_0}=-1.0\times10^{-2}$ m s^{-1}. The dimensionless parameters of the problem are respectively the initial Reynolds, Mach and Prandtl numbers $\mathrm{Re}_0=\rho_0u_0L/\mu_0=6.36\times10^{-1}$, $\mathrm{Ma}_0=u_0/c_0=5.37\times10^{-4}$, $\mathrm{Pr}_0=c_p\mu_0/\lambda_0=7.04\times10^{-1}$. Thermodynamic properties are actualized during the simulation according to the perfect gas law.

The analytical solution of the problem can be found from [50]. Under the Stokes hypothesis ($\mathrm{Re}\leq1$), the test case exhibits a linear velocity field $\boldsymbol{v}_y=-v_0y/L$, with a constant velocity divergence $\boldsymbol{\nabla}\cdot\boldsymbol{v}=-v_0/L$. Considering our hypothesis, equation (1a) reduce to $\frac{1}{\rho}\frac{\mathrm{d}\rho}{\mathrm{d}t}=v_0$. After integration, we obtain $\rho/\rho_0=\exp(v_0(t-t_0)/L)$. Using the law of reversible adiabatic process, *i.e.* $p\rho^{-\gamma}=\mathrm{cst}$, and the perfet gas EoS, the thermodynamic solution of the problem starting at $t_0=0$ s reads to

$$p=p_0\exp(\gamma tv_0/L)\,, \tag{20a}$$

$$T=T_0\exp((\gamma-1)tv_0/L)\,, \tag{20b}$$

$$\rho=\rho_0\exp(tv_0/L)\,. \tag{20c}$$

Thermodynamic variables do not vary in space (0D benchmark) allowing temporal convergence study without any effect of spatial error (linear velocity).

For velocity boundary conditions, left and right boundaries have slip conditions, top has a Dirichlet condition for injection $\boldsymbol{v}_{top}=[0,-v_0]^T$ and bottom has a no-slip condition. For temperature boundary conditions, all the boundaries have homogeneous Neumann conditions.

Table 1 presents the temporal convergence study. Temporal second-order is achieved for pressure, density and temperature, for both L_2 and L_∞ norms. We do not present velocity errors in the table because, whatever the time step, the exact velocity is reached as expected with errors close to the resolution tolerance of linear systems (10^{-14}). As the problem is 1D for velocity and 0D for the other variables, conclusions do not change whatever be the mesh size form 8^2 to 128^2. Let us note the significant variations in relative pressure, temperature and density, final values at time $t_f=1\times10^{-1}$ s being 3.0955×10^5 Pa, 4.4755×10^2 K and 3.1988 kg m^{-3}, respectively.

5.2. Linear acoustic pulse propagation

The second test case investigates the isothermal problem of a linear acoustic wave propagation considering an inviscid perfect gas ($\mu=0$) with its EoS

$$\Delta p=c_0^2\Delta\rho\,, \tag{21}$$

where Δp is the pressure perturbation, $\Delta\rho$ is the density perturbation, and $c_0=\sqrt{\gamma RT_0}$ is the constant speed of sound of the medium. This benchmark has been used in the past to test several novel compressible solvers [9, 27, 28, 18, 25, 14], often to carry out temporal convergence studies. Besides its simplicity and the existence of analytical solutions, this case allows a clear evaluation of the numerical diffusion and dispersion of the proposed numerical schemes.

We consider a monodimensional periodic domain of length $L=1$ m. For velocity boundary conditions, left and right boundaries have periodic conditions while top and bottom have slip conditions.

Δt in s	$\|\|\varepsilon_p\|\|_{L_2}$	order	$\|\|\varepsilon_p\|\|_{L_\infty}$	order	$\|\|\varepsilon_T\|\|_{L_2}$	order
4.00×10^{-4}	1.352×10^{-2}	n/a	1.352×10^{1}	n/a	3.278×10^{-7}	n/a
2.00×10^{-4}	3.389×10^{-3}	1.996	3.389	1.996	8.157×10^{-8}	2.007
1.00×10^{-4}	8.482×10^{-4}	1.998	8.483×10^{-1}	1.998	2.037×10^{-8}	2.001
5.00×10^{-5}	2.120×10^{-4}	2.000	2.121×10^{-1}	2.000	5.144×10^{-9}	1.986
2.50×10^{-5}	5.284×10^{-5}	2.004	5.294×10^{-2}	2.002	1.339×10^{-9}	1.942
1.25×10^{-5}	1.304×10^{-5}	2.019	1.314×10^{-2}	2.010	3.859×10^{-10}	1.794

Δt in s	$\|\|\varepsilon_T\|\|_{L_\infty}$	order	$\|\|\varepsilon_\rho\|\|_{L_2}$	order	$\|\|\varepsilon_\rho\|\|_{L_\infty}$	order
4.00×10^{-4}	3.278×10^{-4}	n/a	1.076×10^{-7}	n/a	1.076×10^{-4}	n/a
2.00×10^{-4}	8.157×10^{-5}	2.007	2.696×10^{-8}	1.996	2.696×10^{-5}	1.996
1.00×10^{-4}	2.038×10^{-5}	2.001	6.749×10^{-9}	1.998	6.750×10^{-6}	1.998
5.00×10^{-5}	5.150×10^{-6}	1.984	1.687×10^{-9}	2.000	1.688×10^{-6}	1.999
2.50×10^{-5}	1.345×10^{-6}	1.937	4.209×10^{-10}	2.003	4.218×10^{-7}	2.001
1.25×10^{-5}	3.924×10^{-7}	1.777	1.043×10^{-10}	2.013	1.051×10^{-7}	2.004

Table 1: IPCMSF temporal order accuracy of the isentropic injection test case. First time step $\Delta t = 4\times10^{-4}$ s equal to $\mathrm{CFL_{ac}} = 1.78\times10^{4}$. Mesh size 128^2, $t_f = 1\times10^{-1}$ s.

At initial time, we consider the thermodynamic state $(T_0, p_0, \rho_0) = (300\mathrm{K}, 10^5\mathrm{Pa}, \frac{p_0}{RT_0})$ and a Gaussian acoustic pressure wave defined as

$$p(x, t_0) = p_0 + \Delta p_0 \exp(-\frac{x^2}{2\Sigma^2}), \tag{22}$$

with Δp_0 the pulse amplitude and Σ a pulse length control parameter. The initial parameter of the pulse is set to $\Delta p_0 = 10^2$ Pa and $\Sigma = 0.1$ m like in [25]. The dimensionless parameters of the problem are respectively $\mathrm{Re}_0 = \infty$ and $\mathrm{Ma}_0 = 7.14\times10^{-4}$.

From the resolution of the d'Alembert equation, analytical solutions are available for all fields. The pressure, density and velocity solutions are respectively

$$p(x,t) = p_0 + \Delta p_0 \exp\left(-\frac{(x - c_0 t)^2}{2\Sigma^2}\right), \tag{23}$$

$$\rho(x,t) = \rho_0 + \frac{\Delta p_0}{c_0^2} \exp\left(-\frac{(x - c_0 t)^2}{2\Sigma^2}\right), \tag{24}$$

$$u(x,t) = \frac{\Delta p_0}{\rho_0 c_0^2} \exp\left(-\frac{(x - c_0 t)^2}{2\Sigma^2}\right). \tag{25}$$

with $c_0 t$ the distance travelled by the wave.

Figure 1a presents a graphical temporal convergence study of the relative pressure field at $t_f = c_0/L = 2.88\times10^{-3}$ s (time travelled by the wave until it returns to its initial position) for various acoustic Courant number, noted $\mathrm{CFL_{ac}} = c_0 \Delta t/\Delta x$. The implicit treatment of pressure increment avoids a stability limitation related to acoustic time step as we do not find any stability limit (still stable at $\mathrm{CFL_{ac}} \sim 4\times10^3$ data not shown). For very large $\mathrm{CFL_{ac}}$ and Euler backward temporal scheme, the acoustic wave is totally diffused but, note that for $\mathrm{CFL_{ac}} = 4.8$ the wave is still well predicted. We observe the relative low diffusivity of the first-order temporal scheme Euler backward at $\mathrm{CFL_{ac}} = 4$ compared to literature results [25] (see $\mathrm{CFL_{ac}} = 0.5$ digitized curve from [25] in Fig. 1a).

Additionally, in Fig. 1b, it is noteworthy that the BDF2 scheme, with second-order temporal accuracy, exhibits significantly lower numerical diffusion compared to the Euler scheme. This results in a pressure profile that closely aligns with the exact solution at $\mathrm{CFL_{ac}} = 2$. An error of less than 1% is observed compared to 20% with the Euler scheme. Using the BDF2 temporal scheme, the correct observation of acoustic propagation is possible while considering $\mathrm{CFL_{ac}}$ greater than unity at the price of increasingly dispersion of the travelling wave (see Fig. 1b for $\mathrm{CFL_{ac}} = 8$).

In Table 2, the temporal convergence study of this test case with the BDF2 scheme is presented with a final time $t_f = L/c_s = 2.88\times10^{-3}$ s. Second-order temporal convergence is confirmed for

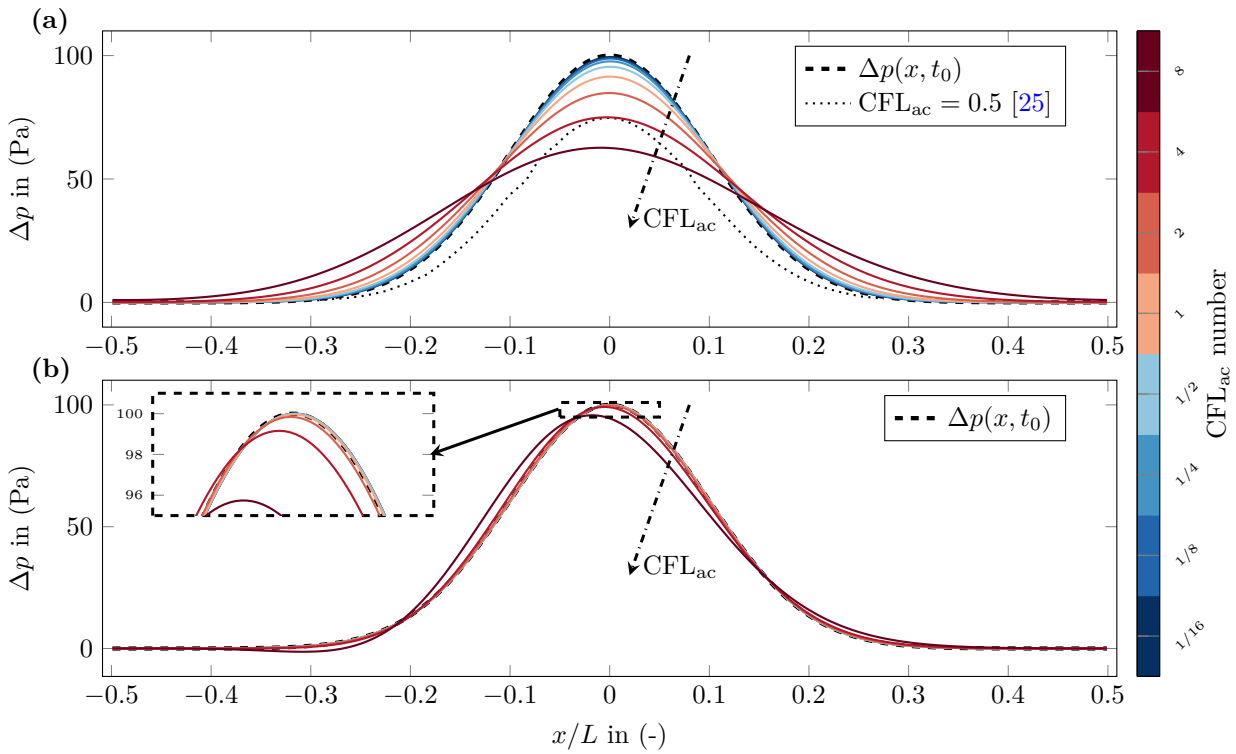

Figure 1: Acoustic pressure field variation at initial state $t = 0$ s (dashed line) and at $t_f = 2.88{\times}10^{-3}$ s for various $\mathrm{CFL_{ac}} = \Delta t c_0/\Delta x$ (solid line colored by CFL value). IPCMSF with (a) Euler backward temporal scheme. (b) BDF2 temporal scheme. Mesh size 512x8.

Δt in s	$\|\|\varepsilon_v\|\|_{L_2}$	order	$\|\|\varepsilon_v\|\|_{L_\infty}$	order	$\|\|\varepsilon_p\|\|_{L_2}$	order
1.60×10^{-4}	4.568×10^{-2}	n/a	9.698×10^{-2}	n/a	1.842×10^{1}	n/a
8.00×10^{-5}	2.304×10^{-2}	0.987	5.057×10^{-2}	0.939	9.293	0.987
4.00×10^{-5}	7.871×10^{-3}	1.550	1.846×10^{-2}	1.454	3.176	1.549
2.00×10^{-5}	1.986×10^{-3}	1.987	4.873×10^{-3}	1.922	8.017×10^{-1}	1.986
1.00×10^{-5}	3.272×10^{-4}	2.601	7.510×10^{-4}	2.698	1.321×10^{-1}	2.601

Δt in s	$\|\|\varepsilon_p\|\|_{L_\infty}$	order	$\|\|\varepsilon_\rho\|\|_{L_2}$	order	$\|\|\varepsilon_\rho\|\|_{L_\infty}$	order
1.60×10^{-4}	3.911×10^{1}	n/a	1.528×10^{-4}	n/a	3.245×10^{-4}	n/a
8.00×10^{-5}	2.039×10^{1}	0.940	7.710×10^{-5}	0.987	1.692×10^{-4}	0.940
4.00×10^{-5}	7.451	1.452	2.635×10^{-5}	1.549	6.182×10^{-5}	1.452
2.00×10^{-5}	1.968	1.920	6.651×10^{-6}	1.986	1.633×10^{-5}	1.920
1.00×10^{-5}	3.036×10^{-1}	2.697	1.096×10^{-6}	2.601	2.519×10^{-6}	2.697

Table 2: IPCMSF temporal order accuracy of the linear acoustic pulse test case. First time step $\Delta t = 1.6\times10^{-4}$ s equal to $\mathrm{CFL_{ac}} = 2.84\times10^{1}$. Mesh size 512×8, $t_f = 2.88\times10^{-3}$ s.

Mesh	$\|\|\varepsilon_v\|\|_{L_2}$	order	$\|\|\varepsilon_v\|\|_{L_\infty}$	order	$\|\|\varepsilon_p\|\|_{L_2}$	order
16x8	5.723×10^{-2}	n/a	1.115×10^{-1}	n/a	2.308×10^{1}	n/a
32x8	3.040×10^{-2}	0.913	6.849×10^{-2}	0.704	1.226×10^{1}	0.913
64x8	1.089×10^{-2}	1.481	2.650×10^{-2}	1.370	4.394	1.481
128x8	2.852×10^{-3}	1.933	6.872×10^{-3}	1.947	1.151	1.932
256x8	5.231×10^{-4}	2.446	1.181×10^{-3}	2.540	2.113×10^{-1}	2.446
512x8	1.382×10^{-4}	1.921	2.832×10^{-4}	2.061	5.567×10^{-2}	1.924

Mesh	$\|\|\varepsilon_p\|\|_{L_\infty}$	order	$\|\|\varepsilon_\rho\|\|_{L_2}$	order	$\|\|\varepsilon_\rho\|\|_{L_\infty}$	order
16x8	4.378×10^{1}	n/a	1.915×10^{-4}	n/a	3.632×10^{-4}	n/a
32x8	2.804×10^{1}	0.643	1.017×10^{-4}	0.913	2.326×10^{-4}	0.643
64x8	1.067×10^{1}	1.394	3.645×10^{-5}	1.481	8.853×10^{-5}	1.394
128x8	2.768	1.947	9.550×10^{-6}	1.932	2.296×10^{-5}	1.947
256x8	4.768×10^{-1}	2.537	1.753×10^{-6}	2.446	3.955×10^{-6}	2.537
512x8	1.140×10^{-1}	2.064	4.619×10^{-7}	1.924	9.457×10^{-7}	2.064

Table 3: IPCMSF spatial order accuracy of the linear acoustic pulse test case. $\mathrm{CFL_{ac}} = 1$, $t_f = 2.88\times10^{-3}$ s.

pressure, velocity, and density, for both L_2 and L_∞ norms. The PCMSF/IPCMSF comparison (data not shown in Appendix D) gives again very close results for error magnitudes as well as second-order temporal convergence for all the solved fields. No pressure accuracy limitation is found when using the *non-incremental* method. We also present in Tab. 3 the spatial convergence study with a constant $\mathrm{CFL_{ac}} = 1$. Second-order spatial convergence is confirmed for all fields considering both L_2 and L_∞ norms.

5.3. Manufactured solutions

The technique known as the method of manufactured solutions involves the development of an *a priori* known analytical solutions for the governing equations. The procedure introduces modifications of the original equations (1) by adding source term on the right-hand side of equations (see Appendix B). These source terms are considered as input, for reproducing the manufactured solution.

In literature, few manufactured solutions for compressible subsonic flows have been developed [51, 29, 30, 13] to validate algorithms. After a detailed analysis of the nature and properties of already proposed solutions, we aim to define a generic, well posed, and reproducible manufactured solution (see Appendix B). We thus propose the following two-dimensional compressible Navier–Stokes solution for a perfect gas in a square domain $\Omega = [0,1]\times[0,1]$ where the pressure $p(x,y,t)$, the temperature

$T(x,y,t)$, the density $\rho(x,y,t)$ and the velocity $\boldsymbol{u}=(u,v)^T$ read to

$$p = p_0 + p_1 \sin(\pi y)\sin(\pi x)\cos(2\pi f t)\,, \tag{26a}$$
$$T = T_0 + T_1 \sin(\pi y)\cos(\pi x)\cos(2\pi f t)\,, \tag{26b}$$
$$\rho = p/RT\,, \tag{26c}$$
$$u = u_0 \sin^2(\pi x)\sin(2\pi y)\cos(2\pi f t)\,, \tag{26d}$$
$$v = u_0 \sin(2\pi x)\sin^2(\pi y)\cos(2\pi f t)\,, \tag{26e}$$

with f the frequency in Hz, p_0 and p_1 the reference and fluctuation pressure in Pa, T_0 and T_1 the reference and fluctuation temperature K, u_0 the reference velocity in $\mathrm{m\,s^{-1}}$ and R the universal gas constant in $\mathrm{J\,K^{-1}\,kg^{-1}}$. The perfect gas EoS permits the verification of the solver with time- and space-dependent material properties, except for dynamic viscosity and conductivity considered as constant here.

The proposed solution is derived from the manufactured solution initially proposed for incompressible flows [22]. One notices good properties of the solution to simulate a subsonic flow with incremental pressure correction method as the non-zero pressure gradient at boundary or the non-zero divergence field. Time-dependent Dirichlet boundary conditions are applied for temperature fields. For velocity boundary conditions, all the boundaries have no-slip conditions while Neumann homogeneous boundary condition is imposed on pressure increment.

To investigate the accuracy of the resolved fields and different ranges of dimensionless parameters, three specific manufactured solutions are introduced in the following three subsections by tuning parameters. It is helpful to test the proposed method on low Mach solution as encountered in compressible natural flows (*e.g.* $\mathrm{Ma}_0 \simeq 1\times10^{-3}$), as well as on solution with much larger Mach (*e.g.* $\mathrm{Ma}_0 \simeq 0.6$), The following parameters will remain constant for all three cases : $f=700$ Hz, $p_0=10^5$ Pa, $p_1=2\times10^3$ Pa, $T_0=300$K, $R=287$ $\mathrm{J\,K^{-1}\,kg^{-1}}$, $\gamma=1.4$. $\mu=1.85\times10^{-5}$ Pa s. All the convergence studies consider the final time $t_f=2\times10^{-3}$ s corresponding to more than one and a half times the period $T=1/f$.

5.3.1. Isothermal high Mach subsonic manufactured solution

The isothermal flow case considers the following parameters $T_1=0$ K, $u_0=200$ $\mathrm{m\,s^{-1}}$. We present this unsteady flow solution for whoever wants to analyse the temporal order without considering the coupling of the Navier–Stokes equations and the energy equation. The dimensionless parameters of this case are $\mathrm{Re}_0=1.26\times10^7$, $\mathrm{Ma}_0=5.76\times10^{-1}$.

Table 4 presents the temporal convergence study. Second-order convergence in time is achieved for velocity, pressure, and density, considering both the L_2 and L_∞ norms.

5.3.2. Anisothermal high Mach subsonic manufactured solution

A fully compressible subsonic case is now studied considering the following parameters $T_1=40$ K, $u_0=200$ $\mathrm{m\,s^{-1}}$, $\lambda=10^{-2}\mathrm{W\,m^{-1}\,K^{-1}}$. We investigate temporal order of convergence on a test case with the following dimensionless parameters: $\mathrm{Re}_0=1.26\times10^7$, $\mathrm{Ma}_0=5.76\times10^{-1}$ and $\mathrm{Pr}_0=1.86$.

Firstly, we present in Fig 2 the variations of the primitive variables of the proposed anisothermal manufactured solution. Fig 2a,b,c,d show respectively pressure, temperature, divergence and velocity fields while Fig 2e,f present respectively the local variations of Mach and Reynolds numbers. One may notice strong divergence variations (see Fig 2c) and a maximal local Mach number at $t=0$ s of 0.6 (see Fig 2e), twice the incompressible limit.

We present in Table 5 the temporal convergence study of the case. The proposed method reaches the temporal second-order for all the resolved fields, for both L_2 and L_∞ norms. We also present in Tab. 6 the spatial convergence study with a constant acoustic Courant number of $\mathrm{CFL_{ac}}=1$ for each simulation necessary to attenuate the temporal error. Second-order spatial convergence is also confirmed for all fields considering both L_2 and L_∞ norms.

5.3.3. Anisothermal low Mach subsonic manufactured solution

A low Mach fully compressible subsonic case in now studied considering the following parameters $T_1=40$ K, $u_0=2$ $\mathrm{m\,s^{-1}}$, $\lambda=10^{-2}$ $\mathrm{W\,m^{-1}\,K^{-1}}$. We investigate temporal order of convergence on a test case with the following dimensionless parameters: $\mathrm{Re}_0=1.26\times10^5$, $\mathrm{Ma}_0=5.76\times10^{-3}$ and $\mathrm{Pr}_0=1.86$,

We present in Table 7 the temporal convergence study of the case. The method reaches the temporal second-order for all the resolved fields, for both L_2 and L_∞ norms.

Δt in s	$\|\|\varepsilon_v\|\|_{L_2}$	order	$\|\|\varepsilon_v\|\|_{L_\infty}$	order	$\|\|\varepsilon_p\|\|_{L_2}$	order
2.00×10^{-4}	3.932×10^{1}	n/a	6.442×10^{1}	n/a	5.853×10^{3}	n/a
1.00×10^{-4}	1.497×10^{1}	1.393	2.570×10^{1}	1.326	1.861×10^{3}	1.653
5.00×10^{-5}	4.289	1.803	7.931	1.696	5.325×10^{2}	1.805
2.50×10^{-5}	1.120	1.938	2.116	1.906	1.402×10^{2}	1.925
1.25×10^{-5}	2.882×10^{-1}	1.958	5.489×10^{-1}	1.947	3.594×10^{1}	1.964
6.25×10^{-6}	7.739×10^{-2}	1.897	1.479×10^{-1}	1.892	9.641	1.898

Δt in s	$\|\|\varepsilon_p\|\|_{L_\infty}$	order	$\|\|\varepsilon_\rho\|\|_{L_2}$	order	$\|\|\varepsilon_\rho\|\|_{L_\infty}$	order
2.00×10^{-4}	1.467×10^{4}	n/a	6.798×10^{-2}	n/a	1.704×10^{-1}	n/a
1.00×10^{-4}	4.935×10^{3}	1.572	2.161×10^{-2}	1.653	5.731×10^{-2}	1.572
5.00×10^{-5}	1.625×10^{3}	1.602	6.185×10^{-3}	1.805	1.887×10^{-2}	1.602
2.50×10^{-5}	4.387×10^{2}	1.889	1.629×10^{-3}	1.925	5.095×10^{-3}	1.889
1.25×10^{-5}	1.131×10^{2}	1.956	4.175×10^{-4}	1.964	1.313×10^{-3}	1.956
6.25×10^{-6}	3.006×10^{1}	1.911	1.120×10^{-4}	1.898	3.492×10^{-4}	1.911

Table 4: IPCMSF temporal order accuracy of the isothermal high Mach manufactured solution. First time step $\Delta t = 2\times10^{-4}$ s equal to $\mathrm{CFL_{ac}} = 1.78\times10^{1}$. Mesh size 256^2 and $t_f = 2\times10^{-3}$ s.

Δt in s	$\|\|\varepsilon_v\|\|_{L_2}$	order	$\|\|\varepsilon_v\|\|_{L_\infty}$	order	$\|\|\varepsilon_p\|\|_{L_2}$	order	$\|\|\varepsilon_p\|\|_{L_\infty}$	order
2.00×10^{-4}	3.753×10^{1}	n/a	7.456×10^{1}	n/a	6.230×10^{3}	n/a	1.975×10^{4}	n/a
1.00×10^{-4}	1.366×10^{1}	1.458	2.493×10^{1}	1.581	1.885×10^{3}	1.724	5.279×10^{3}	1.904
5.00×10^{-5}	3.874	1.818	6.912	1.851	5.200×10^{2}	1.858	1.548×10^{3}	1.770
2.50×10^{-5}	1.012	1.936	1.843	1.907	1.352×10^{2}	1.944	4.014×10^{2}	1.947
1.25×10^{-5}	2.599×10^{-1}	1.961	4.825×10^{-1}	1.934	3.437×10^{1}	1.975	1.054×10^{2}	1.929
6.25×10^{-6}	6.908×10^{-2}	1.912	1.317×10^{-1}	1.873	9.054	1.925	2.831×10^{1}	1.897

Δt in s	$\|\|\varepsilon_T\|\|_{L_2}$	order	$\|\|\varepsilon_T\|\|_{L_\infty}$	order	$\|\|\varepsilon_\rho\|\|_{L_2}$	order	$\|\|\varepsilon_\rho\|\|_{L_\infty}$	order
2.00×10^{-4}	7.616	n/a	3.153×10^{1}	n/a	5.457×10^{-2}	n/a	1.978×10^{-1}	n/a
1.00×10^{-4}	2.519	1.596	8.642	1.867	1.711×10^{-2}	1.673	4.450×10^{-2}	2.152
5.00×10^{-5}	6.835×10^{-1}	1.882	2.403	1.847	4.728×10^{-3}	1.856	1.385×10^{-2}	1.684
2.50×10^{-5}	1.767×10^{-1}	1.952	6.303×10^{-1}	1.931	1.234×10^{-3}	1.938	4.005×10^{-3}	1.790
1.25×10^{-5}	4.528×10^{-2}	1.964	1.616×10^{-1}	1.964	3.158×10^{-4}	1.966	1.065×10^{-3}	1.911
6.25×10^{-6}	1.222×10^{-2}	1.890	4.285×10^{-2}	1.915	8.401×10^{-5}	1.910	2.865×10^{-4}	1.894

Table 5: IPCMSF temporal order accuracy of the anisothermal high Mach subsonic manufactured solution. First time step $\Delta t = 2\times10^{-4}$ s equal to $\mathrm{CFL_{ac}} = 1.78\times10^{1}$. Mesh size 256^2 and $t_f = 2\times10^{-3}$ s.

Mesh	$\|\|\varepsilon_v\|\|_{L_2}$	order	$\|\|\varepsilon_v\|\|_{L_\infty}$	order	$\|\|\varepsilon_p\|\|_{L_2}$	order	$\|\|\varepsilon_p\|\|_{L_\infty}$	order
64x64	3.055	n/a	5.712	n/a	3.811×10^{2}	n/a	1.125×10^{3}	n/a
128x128	8.000×10^{-1}	1.933	1.517	1.913	9.913×10^{1}	1.943	3.041×10^{2}	1.888
256x256	2.022×10^{-1}	1.984	3.911×10^{-1}	1.956	2.494×10^{1}	1.991	7.787×10^{1}	1.965
512x512	5.094×10^{-2}	1.989	9.963×10^{-2}	1.973	6.254	1.995	2.035×10^{1}	1.936

Mesh	$\|\|\varepsilon_T\|\|_{L_2}$	order	$\|\|\varepsilon_T\|\|_{L_\infty}$	order	$\|\|\varepsilon_\rho\|\|_{L_2}$	order	$\|\|\varepsilon_\rho\|\|_{L_\infty}$	order
64x64	5.259×10^{-1}	n/a	1.835	n/a	3.572×10^{-3}	n/a	1.088×10^{-2}	n/a
128x128	1.348×10^{-1}	1.963	4.789×10^{-1}	1.938	9.270×10^{-4}	1.946	3.054×10^{-3}	1.833
256x256	3.394×10^{-2}	1.990	1.216×10^{-1}	1.978	2.338×10^{-4}	1.987	8.115×10^{-4}	1.912
512x512	8.539×10^{-3}	1.991	3.841×10^{-2}	1.662	5.892×10^{-5}	1.988	2.805×10^{-4}	1.533

Table 6: IPCMSF spatial order accuracy of the anisothermal high Mach subsonic manufactured solution. $\mathrm{CFL_{ac}} = 1$ and $t_f = 2\times10^{-3}$ s.

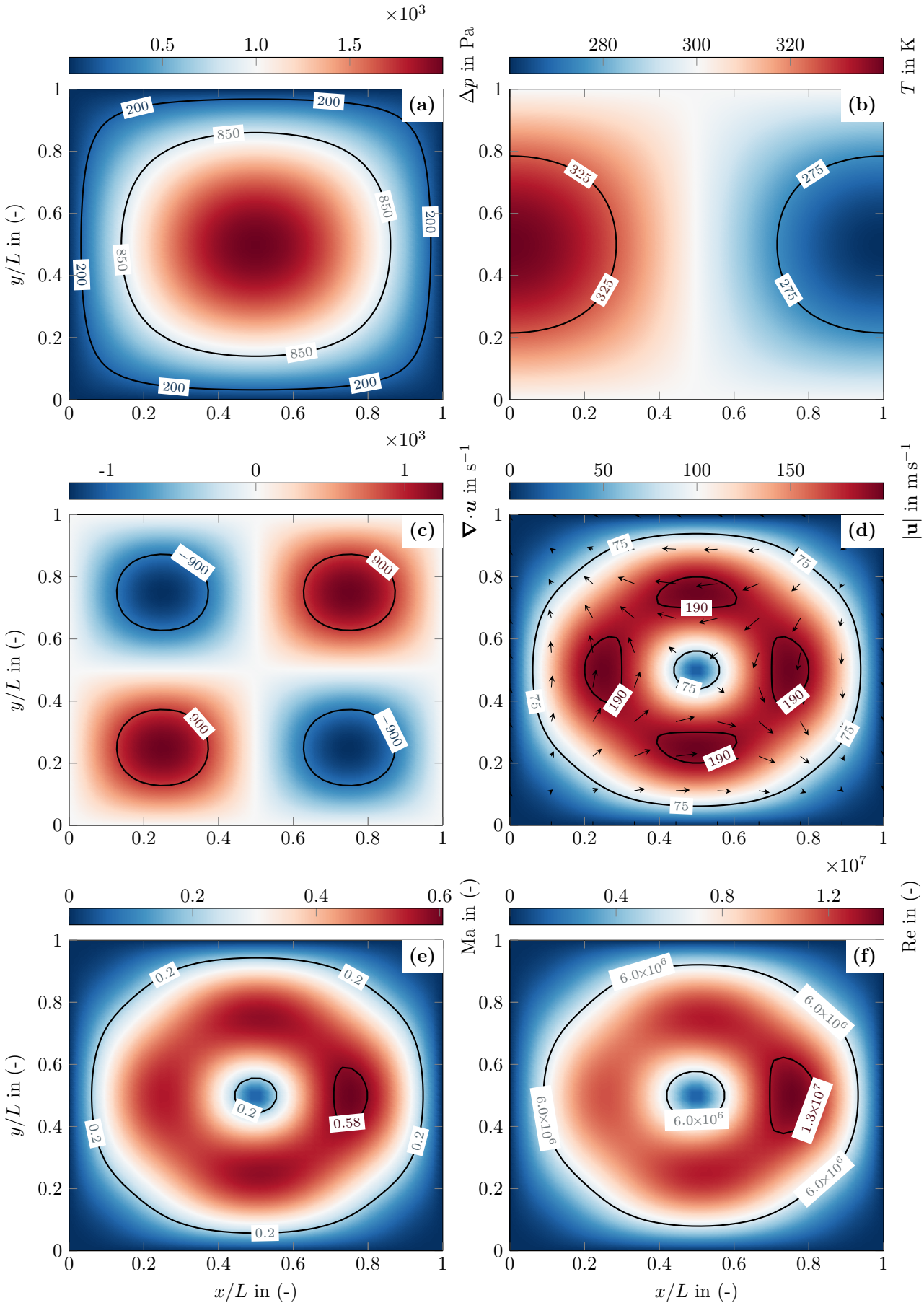

Figure 2: Visualisation of the high Mach anisothermal solution within the square domain $\Omega = [0,1] \times [0,1]$ at $t = 0$ s. (a) Relative pressure field $\Delta p = p - p_0$. (b) Temperature field T. (c) Divergence of the velocity field $\boldsymbol{\nabla} \cdot \boldsymbol{u}$. (d) Velocity vector field $\boldsymbol{u}$ (arrows) and its magnitude $||\boldsymbol{u}||$. (e) Local Mach number Ma. (f) Local Reynolds number Re.

Δt in s	$\|\|\varepsilon_v\|\|_{L_2}$	order	$\|\|\varepsilon_v\|\|_{L_\infty}$	order	$\|\|\varepsilon_p\|\|_{L_2}$	order	$\|\|\varepsilon_p\|\|_{L_\infty}$	order
2.00×10^{-4}	3.731×10^{-1}	n/a	8.833×10^{-1}	n/a	2.155×10^{2}	n/a	4.504×10^{2}	n/a
1.00×10^{-4}	1.391×10^{-1}	1.423	3.183×10^{-1}	1.473	6.530×10^{1}	1.723	1.550×10^{2}	1.539
5.00×10^{-5}	4.110×10^{-2}	1.759	9.129×10^{-2}	1.802	1.830×10^{1}	1.835	5.251×10^{1}	1.562
2.50×10^{-5}	1.100×10^{-2}	1.902	2.372×10^{-2}	1.945	4.732	1.952	1.428×10^{1}	1.879
1.25×10^{-5}	2.825×10^{-3}	1.961	6.062×10^{-3}	1.968	1.192	1.989	3.631	1.976
6.25×10^{-6}	7.200×10^{-4}	1.972	1.530×10^{-3}	1.986	2.997×10^{-1}	1.992	9.187×10^{-1}	1.983

Δt in s	$\|\|\varepsilon_T\|\|_{L_2}$	order	$\|\|\varepsilon_T\|\|_{L_\infty}$	order	$\|\|\varepsilon_\rho\|\|_{L_2}$	order	$\|\|\varepsilon_\rho\|\|_{L_\infty}$	order
2.00×10^{-4}	4.166	n/a	1.349×10^{1}	n/a	1.857×10^{-2}	n/a	6.571×10^{-2}	n/a
1.00×10^{-4}	8.746×10^{-1}	2.252	2.499	2.432	3.712×10^{-3}	2.323	1.190×10^{-2}	2.465
5.00×10^{-5}	1.903×10^{-1}	2.201	4.336×10^{-1}	2.527	7.821×10^{-4}	2.247	2.100×10^{-3}	2.503
2.50×10^{-5}	4.570×10^{-2}	2.058	1.172×10^{-1}	1.888	1.819×10^{-4}	2.104	5.127×10^{-4}	2.034
1.25×10^{-5}	1.140×10^{-2}	2.003	3.193×10^{-2}	1.875	4.441×10^{-5}	2.034	1.371×10^{-4}	1.903
6.25×10^{-6}	2.861×10^{-3}	1.994	8.320×10^{-3}	1.940	1.102×10^{-5}	2.010	3.541×10^{-5}	1.953

Table 7: IPCMSF temporal order accuracy of the anisothermal low Mach manufactured solution. First time step $\Delta t = 2\times10^{-4}$ s equal to $\mathrm{CFL_{ac}} = 1.78\times10^{1}$. Mesh size 256^2 and $t_f = 2\times10^{-3}$ s.

5.4. Comparison between non-incremental and incremental pressure correction method for subsonic compressible flows

For all the verification test cases presented in the present work, we find almost the same behaviour whether solving the pressure p (PCMSF) or the pressure increment φ (IPCMSF) (see Appendix D).

We note that even in the presented manufactured solution problems, specifically designed to challenge the methods by introducing discrepancies at the domain boundaries (where the methods enforce homogeneous Neumann while the solution does not), no difference in both temporal order convergences and error magnitudes are observed between IPCMSF and PCMSF for all the resolved fields (see Table D.17, D.16 and D.18).

The classical pressure accuracy limitations of the *non-incremental* projection method observed in incompressible flows is not present for subsonic compressible flows, as confirmed by our comparison between *non-incremental* and *incremental methods*. These comparable results between the two methods come from the nature of the pressure which is no longer, in compressible flows, only a scalar field allowing to reach the incompressibility constraint but is indeed a dynamic variable with a proper equation (2) which is used to derive the Helmholtz-type equation with variable coefficient (10).

6. Validation

Validation is the process that assesses the extent to which a numerical model accurately represents a physical phenomenon for the purpose of utilizing the results. It entails comparing precise numerical solutions with experimental (or theoretical) results. It's important to note that validation doesn't assume the experimental measurements are inherently more accurate than the numerical solutions; rather, it considers them as the most adequate means available for representing the reality in the context of validation. Benchmarking the numerical solutions obtained with different codes is also a crucial component of the validation process. In this context, the inherent variability of the numerical methods, together with extensive convergence studies, allow to consider the reference numerical solutions as equivalent to experimental measurements.

The validation section is structured around both stationary and unsteady test cases. Initially, the proposed method is validated on a well-known low Mach compressible steady natural convection benchmark, encompassing cases with constant and variable viscosity. Following that, validation is extended to a natural convection test case in the presence of an immersed boundary. In the second part, validation is conducted on two unsteady 1D thermoacoustic wave generation and propagation scenarios. The first involves a Dirichlet boundary condition and a perfect gas, while the second incorporates a heat flux and operates very close to the liquid-vapor critical point. Finally, validation is carried out on a 2D unsteady natural convection case at a Mach number of 0.1. All the benchmarks

presented consider a regime beyond the Boussinesq approximation, commonly referred to as the non-Oberbeck–Boussinesq (NOB) approximation.

6.1. Compressible steady natural convection benchmark

Compressible flows can occur due to large temperature variations resulting in large density changes for which the Boussinesq approximation is no longer valid. In this section, we validate the proposed method by reproducing the classical *case T1* and *case T2* steady-state benchmarks of Le Quéré et al. [10]. From the nomenclature [10], *case T1* refers to constant viscosity and conductivity while the *case T2* considers Sutherland's law for viscosity and conductivity (see Appendix C for parameters values).

We consider a differentially heated square cavity subject to gravitational field $|\boldsymbol{g}| = 9.81\,\mathrm{m\,s^{-2}}$, filled with air considered as a perfect gas, with the following initial dimensionless parameters: temperature ratio $\epsilon = \frac{T_{\mathrm{hot}} - T_{\mathrm{cold}}}{T_{\mathrm{hot}} + T_{\mathrm{cold}}} = 0.6$, Rayleigh number $\mathrm{Ra}_0 = \mathrm{Pr}_0 \frac{g \Delta T L^3 \beta_{p_0} \rho_0^2}{\mu_0^2} = 10^6$, Prandtl number $\mathrm{Pr}_0 = 7.1\times10^{-1}$. Initial Mach number (considering the characteristic velocity $u_0 = \frac{\lambda_0}{\rho_0 c_p L}\sqrt{\mathrm{Ra}_0}$ [52]) are $\mathrm{Ma}_0 = 1.78\times10^{-3}$ for *case T1* and $\mathrm{Ma}_0 = 2.15\times10^{-3}$ for *case T2*, respectively. Due to difference between initial viscosity and conductivity in both cases, the lengths L of the cavities are $L_{\mathrm{T1}} = 4.60\times10^{-2}$ m $L_{\mathrm{T2}} = 6.71\times10^{-2}$ m. The cavity lengths of natural convectioin problmes provided in the article are indicative and must be calculated accurately based on the initial thermophysical state and the value of the Rayleigh number.

The boundary conditions of both cases are as follows. For temperature, the top and bottom walls have adiabatic conditions and left and right are respectively heated and cooled $T_{\mathrm{hot}} = 960$ K and $T_{\mathrm{cold}} = 240$ K. For velocity boundary conditions, all the boundaries have no-slip conditions. Both cases have been simulated considering an adaptative time step driven by a constant $\mathrm{CFL}_{\mathrm{ac}} = 4\times10^2$. The implicit treatment of the pressure computation permits to consider large CFL number which amounts to naturally filtering acoustic waves.

The objective of the present validation is to compare the reference values [10] of the spatial average side walls Nusselt numbers $\overline{\mathrm{Nu}}_{\mathrm{left,right}}$ and cavity pressure at steady state with our simulations. Regarding the previous final time proposed [25], we propose a final time $t_f = 20$ s ensuring the flow reaches a steady state.

Figure 3a,b presents respectively the pseudocolor plot of the temperature field along with the velocity vectors field of the *case T1* and the temperature profile comparison at $y = L/2$ between T1 and T2 cases. Simulation results of the T2 case [53, 54] are also plotted in Fig. 3b. The simulation of *case T2* with our full compressible modelling well reproduces the temperature profile solution [53, 54] while most of the benchmark contributions were obtained considering the low Mach number approximation [10, 54]. To the author's knowledge, temperature profile solution of the *case T1* is unavailable in the literature. We plot in Fig. 3b this horizontal temperature profile and we validate this case in the following regarding Nusselt number and maximal pressure. Regarding the lack of temperature profile data and as this configuration is simpler than T2, this approach is acceptable.

We propose in Table 8 a spatial convergence study of *case T1* for regular meshes at $\mathrm{CFL}_{\mathrm{ac}} = 400$ including Richardson extrapolated values. We observe a spatial second-order convergence on Nusselt numbers, spatially averaged relative pressure, temperature, and velocity magnitude.

Reference values of T1 are $\overline{\mathrm{Nu}} = 8.859\,78$ and $p_{\mathrm{max}}/p_0 = 0.856\,338$ [10]. On the mesh size 1024^2, we found a maximal normalized pressure of $p_{\mathrm{max}}/p_0 = 0.855\,486$ and an absolute difference between left and right Nusselt number of $\overline{\mathrm{Nu}}_L - \overline{\mathrm{Nu}}_R = 9.48\times10^{-5}$ (see Table 8). By carefully reading the list of pitfalls and recommendations proposed by the authors of the benchmark [10], we thus verified the equality (at three significant digits) of both left and right averaged Nusselt number According to reference values [10], the absolute relative differences are respectively 9.95×10^{-2} % for the maximal pressure and 3.76×10^{-2} % for the Nusselt number (left value chosen).

Table 9 shows the spatial convergence study of *case T2* for regular meshes at $\mathrm{CFL}_{\mathrm{ac}} = 400$ also with Richardson extrapolated values. Here, spatial second-order is observed on spatial averaged relative pressure, temperature and velocity, and varying between 1.64 and 1.85 for left and right Nusselt numbers, respectively. Reference values of this case are $\overline{\mathrm{Nu}} = 8.6866$ and $p_{\mathrm{max}}/p_0 = 0.924\,487$ [10]. On the mesh size 1024^2, we found a maximal normalized pressure of $p_{\mathrm{max}}/p_0 = 0.923\,744$ and an absolute difference between left and right Nusselt number of 1.4×10^{-4} (see Table 9). According to reference values [10], the absolute relative differences are respectively 8.03×10^{-2} % for the maximal pressure and 9.01×10^{-3} % for the Nusselt number (left value chosen).

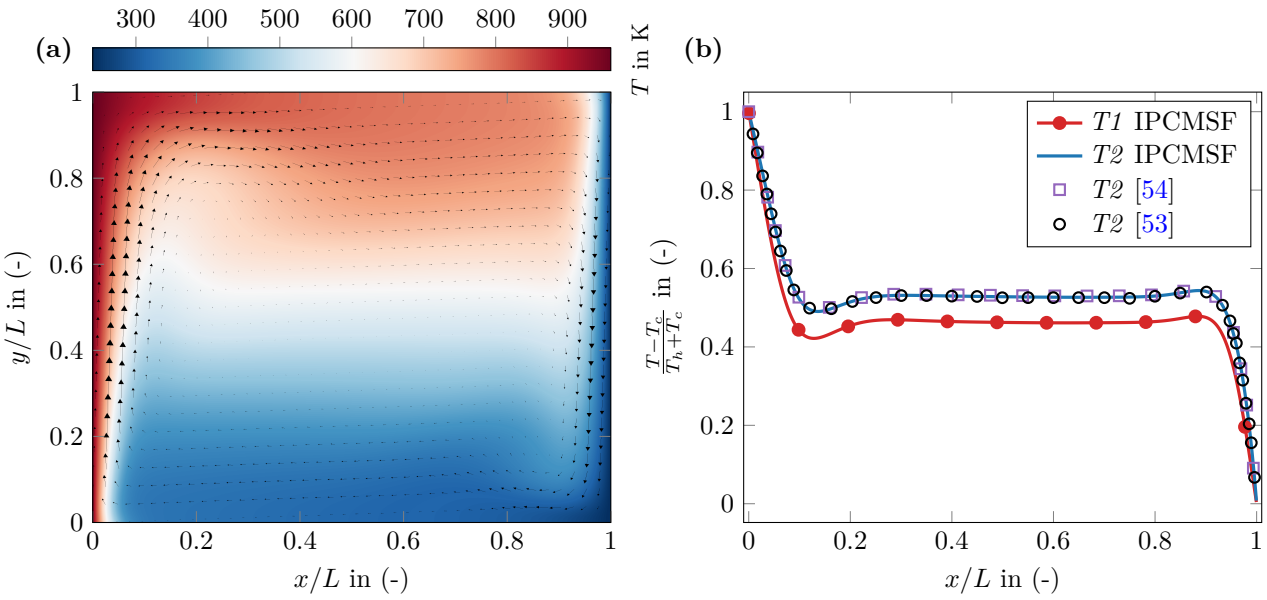

Figure 3: (a) Pseudocolor plot of temperature field and velocity vectors field of the *case T1* [10]. (b) Horizontal dimensionless temperature profile $T(x, y = L/2)/T_0$ comparison between T1 (circle symbols) and T2 (solid line) cases. Vierendeels et al. [53] *case T2* simulation (circle symbols), Kuan and Szmelter [54] *case T2* simulation (rectangle symbols). Simulation results of *case T2* [53, 54] are also plotted in Fig. 3b. $\mathrm{CFL_{ac}} = 400$, mesh size 1024^2, $t_f = 20$ s.

Mesh	$\overline{\mathrm{Nu}}_{\mathrm{left}}$	order	$\overline{\mathrm{Nu}}_{\mathrm{right}}$	order	$\overline{\Delta p}$ in Pa	order
64x64	9.0509	n/a	9.0811	n/a	-1.7907×10^4	n/a
128x128	8.9110	n/a	8.9184	n/a	-1.5438×10^4	n/a
256x256	8.8711	1.810	8.8728	1.834	-1.4809×10^4	1.971
512x512	8.8598	1.821	8.8602	1.864	-1.4669×10^4	2.170
1024x1024	8.8564	1.741	8.8565	1.770	-1.4643×10^4	2.452
Extrapolation	8.8550	n/a	8.8550	n/a	-1.4637×10^4	n/a

Mesh	$\overline{\lvert\boldsymbol{u}\rvert}$ in $\mathrm{m\,s^{-1}}$	order	$\overline{T}$ in K	order
64x64	4.9700×10^{-2}	n/a	5.6453×10^2	n/a
128x128	4.8601×10^{-2}	n/a	5.6823×10^2	n/a
256x256	4.8313×10^{-2}	1.929	5.6930×10^2	1.791
512x512	4.8245×10^{-2}	2.077	5.6957×10^2	1.967
1024x1024	4.8230×10^{-2}	2.183	5.6964×10^2	1.995
Extrapolation	4.8225×10^{-2}	n/a	5.6966×10^2	n/a

Table 8: Spatial order accuracy of the compressible natural convection *case T1* [10] for spatially averaged Nusselt numbers, relative pressure, velocity magnitude and temperature. $\mathrm{CFL_{ac}} = 400$, $t_f = 20$ s. Extrapolated Richardson's values are also given.

Mesh	$\overline{\mathrm{Nu}_{\mathrm{left}}}$	order	$\overline{\mathrm{Nu}_{\mathrm{right}}}$	order	$\overline{\Delta p}$ in Pa	order
64x64	9.0067	n/a	9.0350	n/a	-1.1448×10^{4}	n/a
128x128	8.7767	n/a	8.7881	n/a	-8.9730×10^{3}	n/a
256x256	8.7129	1.852	8.7155	1.765	-8.0069×10^{3}	1.357
512x512	8.6924	1.634	8.6930	1.689	-7.7715×10^{3}	2.037
1024x1024	8.6858	1.644	8.6860	1.682	-7.7269×10^{3}	2.401
Extrapolation	8.6827	n/a	8.6828	n/a	-7.7164×10^{3}	n/a

Mesh	$\overline{\lvert\boldsymbol{u}\rvert}$ in $\mathrm{m\,s^{-1}}$	order	$\overline{T}$ in K	order
64x64	5.6898×10^{-2}	n/a	5.9958×10^{2}	n/a
128x128	5.6037×10^{-2}	n/a	6.0538×10^{2}	n/a
256x256	5.5683×10^{-2}	1.285	6.0746×10^{2}	1.478
512x512	5.5585×10^{-2}	1.848	6.0808×10^{2}	1.740
1024x1024	5.5562×10^{-2}	2.059	6.0825×10^{2}	1.847
Extrapolation	5.5554×10^{-2}	n/a	6.0832×10^{2}	n/a

Table 9: Spatial order accuracy of the compressible natural convection *case T2* [10] for spatially averaged Nusselt numbers, relative pressure, velocity magnitude and temperature. $\mathrm{CFL_{ac}}=400$, $t_f=20$ s. Extrapolated Richardson's values are also given.

To complement the usual data provided for this benchmark, we propose in Fig. 4a the local Mach number at steady state of the *case T1* computed as $\mathrm{Ma}=\sqrt{u^2+v^2}/\sqrt{\gamma RT}$. We observe the maximal Mach number values in the both sidewall boundary layers of $\mathrm{Ma_{max}}=4.5\times10^{-4}$. We do not find back the $\mathrm{Ma_0}$ assumed by the characteristic velocity coming from the current dimensional analysis [52]. The current range of local Mach is one order of magnitude below the expected value, *i.e.* $\mathrm{Ma_0}=1.78\times10^{-3}$. The characteristic velocity overestimates the true characteristic velocity, whether it is calculated [55, 52, 56]. This remark is valid also for the other natural convection benchmarks proposed (Section 6.3.3 and Section 6.2). To emphasize the compressibility of the flow and in addition to the local Mach number of *case T1*, we report the maximum and minimum values of the steady-state velocity divergence $(\boldsymbol{\nabla}\cdot\boldsymbol{v})_{\mathrm{max}}=12.97\ \mathrm{s^{-1}}$ (left bottom of the cavity) and $(\boldsymbol{\nabla}\cdot\boldsymbol{v})_{\mathrm{min}}=-9.57\ \mathrm{s^{-1}}$ (top right of the cavity). For *case T2* we found at same locations $(\boldsymbol{\nabla}\cdot\boldsymbol{v})_{\mathrm{max}}=11.61\ \mathrm{s^{-1}}$ and $(\boldsymbol{\nabla}\cdot\boldsymbol{v})_{\mathrm{min}}=-6.80\ \mathrm{s^{-1}}$.

6.2. Immersed boundary compressible steady natural convection benchmark

Natural convection in a cavity induced by an immersed heating body is considered in this section. The steady case from Bouafia and Daube [55] is considered with the following dimensionless parameters $\mathrm{Ra_0}=5\times10^{6}$, $\mathrm{Re_0}=2.65\times10^{3}$, $\mathrm{Ma_0}=1.53\times10^{-3}$, $\mathrm{Pr_0}=7.1\times10^{-1}$, $\varepsilon=0.2$ with the reference velocity computed as $V_0=\frac{\mu_0}{\rho_0 L}\sqrt{\mathrm{Ra_0}}$ [55]. The fluid filling the square cavity of length $L=7.15\times10^{-2}$ m is air with temperature-dependent viscosity and conductivity following Sutherland's law (see Appendix C for parameters values). We refer the reader to the original paper for the geometrical configuration [55]. We propose for our simulations a constant $\mathrm{CFL_{ac}}=600$ and a final time $t_f=30$ s which verifies the steady state residuals of our simulations. A spatial first-order volume-penalty method is used [38] (see Section 3.4).

For temperature, the top and bottom walls have adiabatic conditions, left and right boundaries are cooled and the immersed boundary is heated ($T_{\mathrm{hot}}=360$ K and $T_{\mathrm{cold}}=240$ K). For velocity boundary conditions, no slip conditions are considered.

Figure 5 present at steady state in (a) the comparison of dimensionless velocity and temperature horizontal profiles and in (b) the pseudocolor plot of temperature field and velocity vectors field. The characteristic flow described by Bouafia and Daube [55], under a low Mach numerical method, is well found back by our simulations with the two counter-rotating recirculation zones cut off by a central plume induced by the heated immersed boundary (see Figure 5b). More importantly, the flow symmetry along the central vertical axis at this Rayleigh number is observed in Fig 5a,b and in Fig 4c. A discrepancy is visible for both velocity and temperature horizontal profiles (Figure 5a) between the literature data [55] and our simulation on the mesh 1024^2. We report that our 1024^2 mesh achieves spatial convergence (see Table 10) and we note that Bouafia's data closely align with our 512^2 mesh (data not shown).

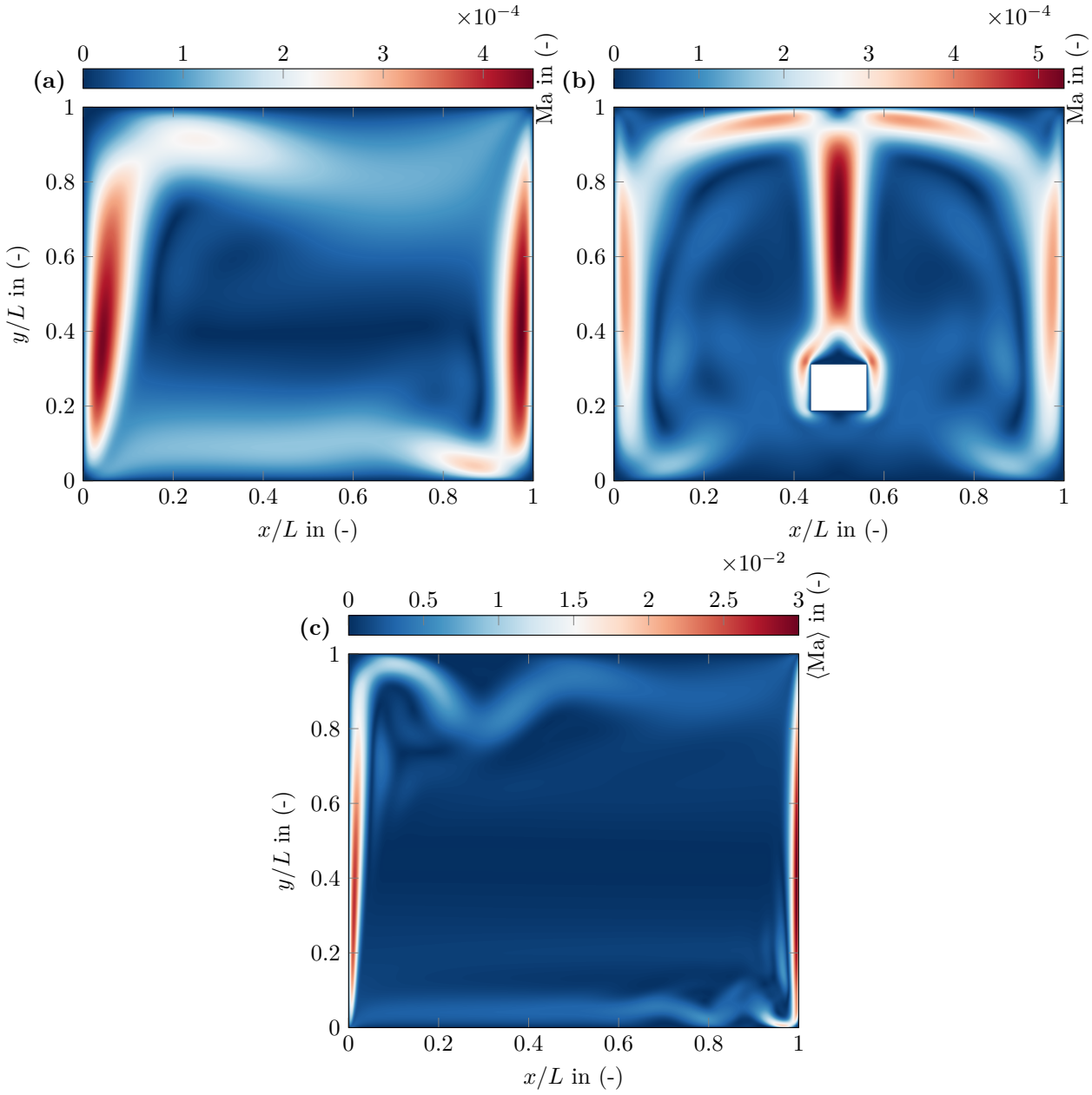

Figure 4: Local Mach number variations. (a) Steady compressible *case T1* benchmark [10]. Mesh size 1024^2, $\mathrm{CFL_{ac}} = 400$, $t_f = 20$ s. (a) Steady immersed boundary compressible benchmark [55]. Mesh size 1024^2, $\mathrm{CFL_{ac}} = 600$, $t_f = 30$ s. (c) Time averaged Mach of the unsteady compressible benchmark [56]. $\mathrm{CFL_{ac}} = 2.5{\times}10^3$, Chebyshev mesh size 256^2, $t_f = 5.0051{\times}10^3$ s.

Mesh	$\overline{\mathrm{Nu}_{\mathrm{left}}}$	order	$\overline{\mathrm{Nu}_{\mathrm{right}}}$	order	$\overline{\Delta p}$ in Pa	order
64x64	6.1463	n/a	6.1463	n/a	-1.3629×10^{4}	n/a
128x128	6.4141	n/a	6.4141	n/a	-1.0808×10^{4}	n/a
256x256	6.5437	1.046	6.5437	1.046	-9.9439×10^{3}	1.706
512x512	6.6131	0.902	6.6131	0.902	-9.5649×10^{3}	1.190
1024x1024	6.6496	0.927	6.6496	0.927	-9.3757×10^{3}	1.003
Extrapolation	6.6901	n/a	6.6901	n/a	-9.1873×10^{3}	n/a

Mesh	$\overline{\lvert\boldsymbol{u}\rvert}$ in $\mathrm{m\,s^{-1}}$	order	$\overline{T}$ in K	order
64x64	3.7092×10^{-2}	n/a	2.6967×10^{2}	n/a
128x128	3.7341×10^{-2}	n/a	2.7219×10^{2}	n/a
256x256	3.7501×10^{-2}	0.633	2.7321×10^{2}	1.291
512x512	3.7575×10^{-2}	1.120	2.7366×10^{2}	1.197
1024x1024	3.7609×10^{-2}	1.099	2.7387×10^{2}	1.088
Extrapolation	3.7640×10^{-2}	n/a	2.7406×10^{2}	n/a

Table 10: Spatial order accuracy of the immersed boundary compressible natural convection [55] for spatially averaged Nusselt numbers, relative pressure, velocity magnitude and temperature. $\mathrm{CFL_{ac}}=600$, $t_f=30$ s. Extrapolated Richardson's values are also given.

We present the local Mach number at steady state in Fig. 4b. The maximum Mach number ($\mathrm{Ma_{max}}=5.3\times10^{-4}$) are located in the area of the central vertical thermal plume. As noted in Section 6.1, the range of local Mach is one order of magnitude below the expected value, *i.e.* $\mathrm{Ma_0}$=1.53×10^{-3}. In addition to the local Mach number and to give another measure of the compressibility of the flow, we report the maximum and minimum values of the velocity divergence at steady state, $(\boldsymbol{\nabla}\cdot\boldsymbol{v})_{\max}=17.27\ \mathrm{s^{-1}}$ and $(\boldsymbol{\nabla}\cdot\boldsymbol{v})_{\min}=-15.07\ \mathrm{s^{-1}}$, located at the two upper corners of the heated immersed boundary.

As expected due to the immersed boundary method used, first convergence order is observed (Table 10) on spatially averaged Nusselt numbers, relative pressure, velocity, and temperature. Richardson extrapolated values are also provided in the table. To the author's knowledge, Nusselt numbers of this benchmark have never been reported, both on the side walls (Table 10), but also on the hot Immersed Boundary (IB), *i.e.* $\mathrm{Nu}^{\mathrm{IB}}_{\mathrm{top}}=1.1680\times10^{1}$, $\mathrm{Nu}^{\mathrm{IB}}_{\mathrm{bottom}}=3.0022\times10^{1}$, $\mathrm{Nu}^{\mathrm{IB}}_{\mathrm{left}}=3.1638\times10^{1}$, $\mathrm{Nu}^{\mathrm{IB}}_{\mathrm{right}}=3.1638\times10^{1}$ on the finest grid. For all Nusselt computations, we consider the length of the cavity as the characteristic length. The high Nusselt numbers of left, right, and bottom IB express the very thin thermal boundary layer observed compared to the top IB thermal boundary layer (see Fig 5b). Absolute difference between left and right Nusselt number for the entire cavity and for the immersed boundary are respectively 1.92×10^{-11} and 4.28×10^{-11}.

6.3. Unsteady test cases

6.3.1. Thermoacoustic wave propagation in a perfect gas

The generation and propagation of thermoacoustic wave is the subject of the present test case introduced by Huang and Bau [57] and later studied by Farouk et al. [58]. A nitrogen-filled one-dimensional cavity of length L=1mm is at the initial state $(T_0,p_0,\rho_0)=(300\mathrm{K},101325\mathrm{Pa},\frac{p_0}{RT_0})$, where the gas is considered to be a perfect gas. The viscosity and conductivity of the fluid are temperature dependent (see Appendix C for parameters values). The validation of this test case is carried out by the comparison of our pressure wave profile at time $t=0.25t_0=7.08\times10^{-7}$ s against reported data from simulations of the original paper [57] and from Farouk et al. [58]. The dimensionless parameters are respectively $\mathrm{Ma_0}=6.0\times10^{-2}$ (computed from velocity max peak at $t=0.25t_0$ and the initial speed of sound $c_0=\sqrt{\gamma RT_0}$) and $\mathrm{Pr_0}=0.75$.

For velocity boundary conditions, left and right boundaries have no-slip conditions while top and bottom boundaries have slip conditions. For temperature boundary conditions, top and bottom have homogeneous Neumann conditions, right and left have respectively Dirichlet condition with $T_R=T_0$ and $T_L(t>0)=2T_0$.

Figure 6 presents the thermoacoustic wave shape within the cavity at $t=0.25t_0$ by plotting the dimensionless relative pressure along space for our simulation and literature data. This flow is char-

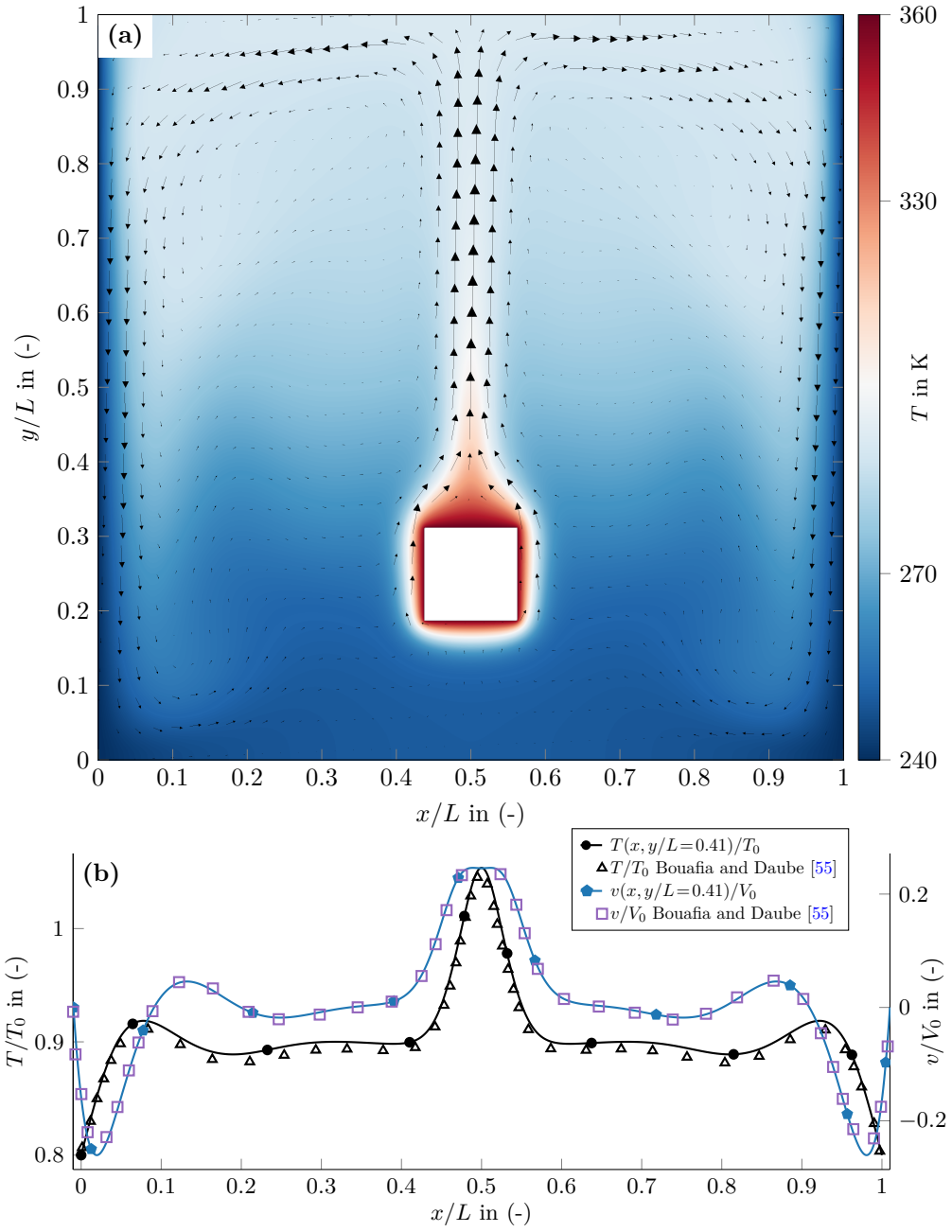

Figure 5: (a) Pseudocolor plot of temperature field and velocity vectors field at stationarity. (b) Horizontal profiles of dimensionless temperature $T(x, y/L = 0.41)/T_0$ (left y-axis) and vertical velocity $v(x, y/L = 0.41)/V_0$ (right y-axis). Mesh size 1024^2, $\mathrm{CFL}_{\mathrm{ac}} = 600$, $t_f = 30$ s.

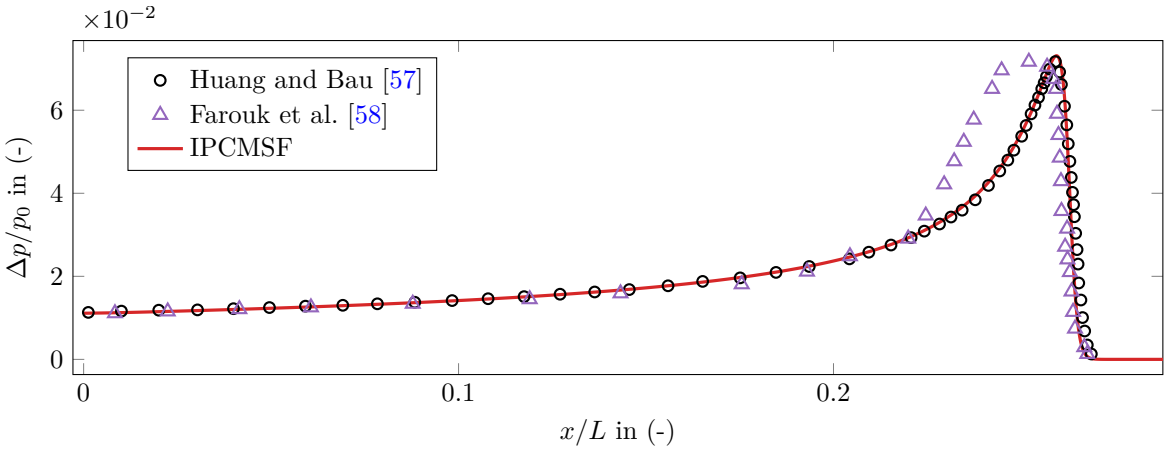

Figure 6: Comparison of dimensionless relative pressure wave at $t = 0.25t_0 = 7.08\times10^{-7}$ s. IPCMSF with BDF2 temporal scheme (solid line), simulation from Huang and Bau [57] (empty circle symbols), simulation from Farouk et al. [58] (empty triangle symbols). Mesh size 32768×8 and $\mathrm{CFL_{ac}}=0.1$.

acterized by the propagation of a pressure wave with a sharp front and an increasing peak width over time [57, 58]. Because of the strong heating on the left of the cavity and the ideal gas hypothesis, the wave speed is variable and its correct prediction is mandatory. An inconsistency between the two references about the wavefront and the speed of the wave can be seen in Fig. 6. The proposed solution (mesh size 32768×8 and $\mathrm{CFL_{ac}}=0.1$), resulting from a spatial and temporal comparative study, can be seen as a reference solution. It is possible to validate the propagation speed of the Huang and Bau [57] wave by comparison with our data. The present benchmark permits to validate our method to simulate thermoacoustic wave propagation. In the next test case, we investigate the same phenomenon very close to the liquid-vapor critical point (where fluid compressibility is very high) with a very low amplitude and sharp thermoacoustic wave propagation.

6.3.2. Thermoacoustic wave propagation close to the liquid-vapor critical point

Miura et al. [59] firstly study experimentally supercritical carbon dioxide acoustic wave propagation using a very sensitive interferometer to capture the piston effect within a cavity of length $L=1.08$ cm. The reproduction of Miura et al. [59] experimental data has been the cornerstone for validation of a CFD code with applications in supercritical fluid dynamics [36, 60, 61]. On the critical isochore and very close to the critical point ($T_c=304.13$ K, $\rho_c=467.6$ kg m^{-3}, $p_c=73.77$ bar), the authors reported the normalized variation of density $\frac{(\rho-\rho_0)}{\rho_0}\times10^7$ along a period of time $t_f=0.4$ ms when the left cavity is heated by a constant heat flux Φ_L during 0.2 ms. After this period, adiabatic condition is imposed to the left wall.

A simulation using initial and boundary conditions closely approximating those of the experimental setup has been conducted within a one-dimensional domain. For the temperature boundary, we impose on the left wall a constant heat flux $\Phi_L=1.83$ kW m^{-2} during the first 0.2 ms and adiabatic condition to the right wall and left wall after $t>0.2$ ms. For the velocity boundary, we impose slip condition to all boundaries. The NIST `refprop` library [62] has been used to compute the density and all the thermophysical properties of the fluid.

According to the experiment and the simulations (see Fig. 7, 8), the wave propagates continuously between the left and right walls. This leads to an increase in bulk temperature and, consequently, an increase in density. The present test case is highly challenging given the very low variations in density (approximately 1×10^{-7}) and the sharp shape of the travelling wave.

Figure 7 presents the normalized density variation at the cell centre as a function of time of the $T_0-T_c=150$ m K experiment of Miura et al. [59]. The results with first-order Euler backward are found to be in good agreement with experimental results, as well as other numerical solutions, validating the proposed method for flows very close to the critical point. Let us note that we simulated this test case with BDF2 temporal scheme at $\mathrm{CFL_{ac}}=1$ but, because of the dispersivity of the scheme (see Fig. 1b) and the sharp shape of the wave, the travelling wave is reconstructed with oscillations.

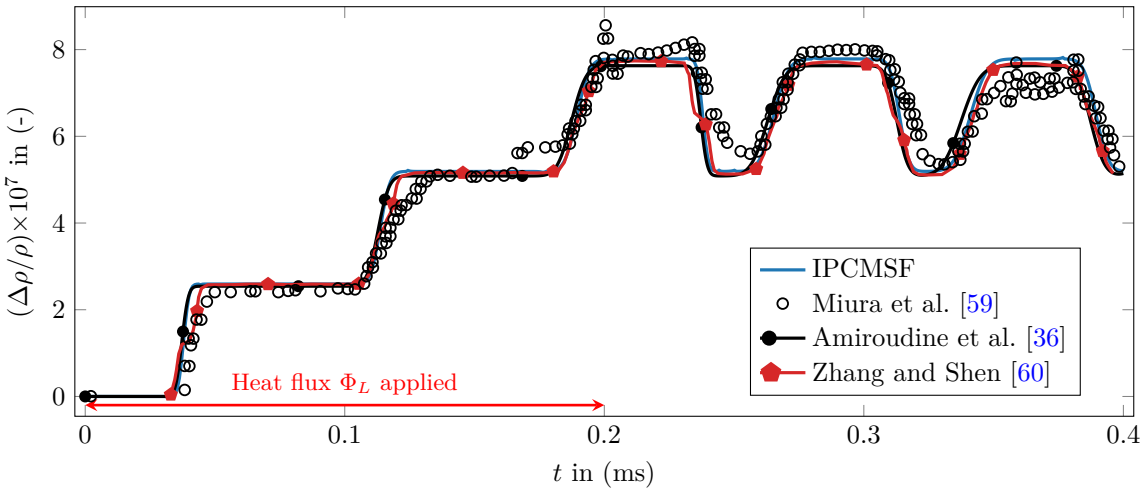

Figure 7: Comparison of normalized density variation between the experimental data at $\Delta T = 150\,\mathrm{m\,K}$ from the critical point and various numerical simulations. Numerized original experimental data [59] (empty circle symbols), IPCMSF with Euler backward temporal scheme (solid line) for a mesh size 1024×8 and $\mathrm{CFL_{ac}} = 1$, Amiroudine et al. [36] simulation (circle symbols), Zhang and Shen [60] simulation (pentagon symbols).

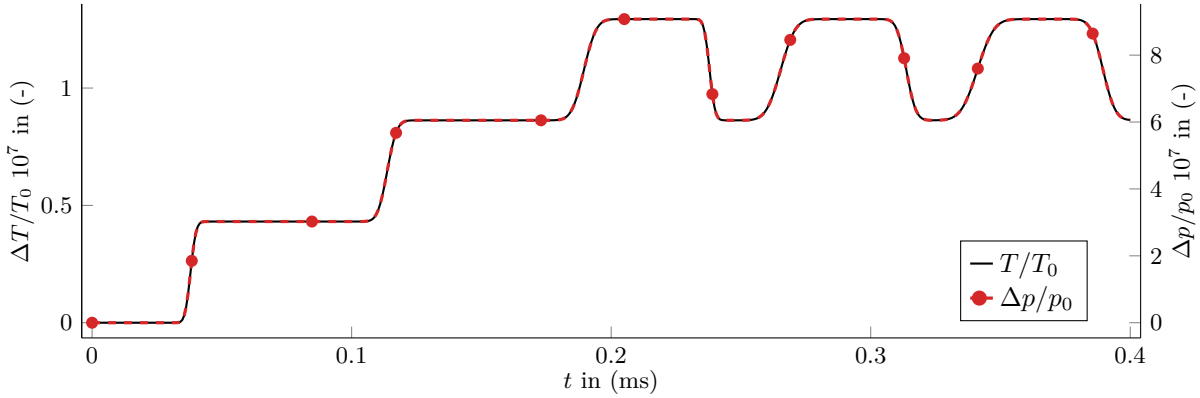

Figure 8: Thermodynamic variations at the cell center during the experiment of Miura et al. [59] at $\Delta T = 150\ \mathrm{m\,K}$ from the critical point. Right y-axis: Normalized relative pressure (dashed line with symbols). Left y-axis: Normalized temperature (solid line). IPCMSF with Euler backward temporal scheme (solid line) for a mesh size 1024×8 and $\mathrm{CFL_{ac}} = 1$,

In addition to the density variations and for the sake of reproducibility, Figure 8 shows the normalized variations of temperature and pressure at the centre of the cell. As we compute density solely from the NIST `refprop` database and given our satisfactory result on the density wave propagation, we deduce that pressure and temperature fields have been very well resolved.

6.3.3. Compressible unsteady natural convection benchmark

The last challenging benchmark addressed by IPCMSF is a recently proposed unsteady differentially heated cavity with large temperature variations problem [56]. A two-dimensional square cavity of length $L = 2.05\times10^2$ m is filled with a perfect gas, where viscosity and conductivity vary according to Sutherland's law (see Appendix C for parameters values). The dimensionless parameters of the reproduced benchmark are $\mathrm{Ra_0} = 1.83\times10^8$, $\mathrm{Re_0} = 1.61\times10^4$, $\mathrm{Ma_0} = 1\times10^{-1}$ (considering the reference velocity $u_0 = \sqrt{2\varepsilon Lg}$ [56]), $\mathrm{Pr_0} = 7.1\times10^{-1}$, $\varepsilon = 0.6$. One can observe significantly larger Mach number compared to the Le Quéré et al. [10] benchmark (see Section 6.1), providing an interesting complementary validation test case for subsonic compressible methods.

Boundary conditions are identical as in Section 6.1. Various strategies exist to avoid the stiff initialization of an abrupt heating of vertical walls that may lead to the divergence of the simulation.

Unlike Farouk et al. [58] which impose time-dependent Dirichlet boundary conditions for temperature ($T_L(t)$ and $T_R(t)$), we propose a geometric time step progression $\Delta t_{n+1} = 1.2\Delta t_n$ from initial state, with a first time step $\Delta t_0 = 10^{-6}$ s, until we reach the CFL_{ac} driven time step. We report no differences induced by both strategies (time-dependent boundary conditions or geometric time step progression) in the periodically established flow solution.

For ease of reproducibility, we provide the starting time for our statistical analysis $t_s/t_{\text{eddy}} = 40$ along with the final time of the simulation $t_f/t_{\text{eddy}} = 100$. The timescale is computed as $t_{\text{eddy}} = 4L/(3u_0)$ [56]. As performed by Wen et al. [56], we obtained a periodically established flow at this final time with relevant statistics of the resolved fields.

Unlike the Le Quéré et al. [10] cases in Section 6.1, comparative results on regular and Chebychev mesh grids point out the necessity of Chebyshev grid refinement to well capture the very thin boundary layer of the case (see Figure 9a,b). We thus present results of the 256^2 Chebyshev mesh with an adaptative time step driven by an acoustic $\text{CFL}_{\text{ac}} = 2.5\times10^3$. A spatial convergence study in shown in Table 11 for various Chebyshev mesh sizes. We report that our presented simulation of 256^2 Chebyshev grid achieves spatial convergence for the presented metrics. The computed minimal Kolmogorov scale reaches the value of 2.58×10^{-1} m and its located within the boundary layer of the right bottom corner (cold wall boundary) as found by Wen et al. [56]. (below the smallest mesh size of 7.77×10^{-3} m). Throughout the domain, we always observe a local Kolmogorov scale larger than the local mesh size, indicating that we accurately capture the flow dynamics.

Figure 9a show the pseudocolor plot of the time averaged temperature , noted $\langle T\rangle$, and the velocity vector field at final time. In addition of the global overview of this natural convection benchmark and in order to provide reproducible data, we propose in Fig 9b three horizontal time averaged temperature profiles at final time along the vertical axis at $y=0.05L$, $y=0.5L$, $y=0.85L$, respectively.

Figure 9c,d show the time evolution of the instantaneous dimensionless temperature and velocity along the last five cycle. The localization of the probes are for the temperature and velocity at $(x=0.85L, y=0.05L)$ and $(x=0.95L, y=0.05L)$, respectively. As found by Wen et al. [56], we find back two periodic signals of period $T = 1.85t_{\text{eddy}}$. Although we use a different numerical method, we observe an instantaneous temperature periodic temporal curve in good agreement with existing result [56]. Regarding the temporal evolution of instantaneous x-velocity (see Fig 9c), our temporal evolution during the period is relatively different from that reported although overall we find similar behaviour. One possible reason is that we are not comparing the temporal evolution of velocity at the exact same position within the cavity. In order to remove possible ambiguity on the location of the probes, we have marked them in Fig 9a.

We present the local time averaged Mach number at $t_f = 5.0051\times10^3$ s in Fig. 4c. The maximum Mach number ($\text{Ma}_{\text{max}} = 3\times10^{-2}$) are located in the both very thin sidewall boundary layers as in Section 6.1. The range of local time averaged Mach is one order of magnitude below the expected value. Wen et al. [56] also document this discrepancy in the Mach order of magnitude on the Ra=5×10^9 case by plotting contour plot of local Mach number. In addition to the local Mach number, we report the maximum and minimum values of the instantaneous velocity divergence at final time, $(\boldsymbol{\nabla}\cdot\boldsymbol{v})_{\text{max}} = 0.62$ s^{-1} (left bottom of the cavity) and $(\boldsymbol{\nabla}\cdot\boldsymbol{v})_{\text{min}} = -0.30$ s^{-1} (right top of the cavity).

From data given by Wen et al. [56], the validation of this test case is achieved by the comparison of (a) the dimensionless temperature and velocity fluctuations spectrums, (b) the left and right time-averaged Nusselt number.

We present in Figure 9e,f the dimensionless Power Density Spectrum (PDS) of the dimensionless velocity and temperature fluctuations fields. The reported dimensionless PDS of a field x is computed as $\text{PDS}_x = |\text{DFT}x|^2/t^2_{\text{eddy}}$ with DFT the Discret Fourier Transform (DFT) of x. For both x-velocity and temperature fluctuations, we found the first four dimensionless frequencies $\boldsymbol{f}\cdot t_{\text{eddy}} = (5.4\times10^{-1}, 1.0, 1.6, 2.2)^T$. Computed frequencies are consistent with reported values [56], *e.g.* the first frequency is for both studies $f_1 t_{\text{eddy}} \simeq 0.5$.

The time averaged left and right Nusselts numbers computed on the last five cycles are respectively $\overline{\text{Nu}}_{\text{left}} = 34.82$, $\overline{\text{Nu}}_{\text{right}} = 34.75$. Our Nusselt numbers are consistent with the left reported value [56] $\overline{\text{Nu}}_{\text{left}} = 34.2718$. These given Nusselt number values are different from those in the Table 11 as $\langle\overline{\text{Nu}}_{\text{left,right}}\rangle$ come from the averaging process from t_s until t_f. The absolute difference between left and right averaged Nusselt over the last five cycles is 7.46×10^{-2}.

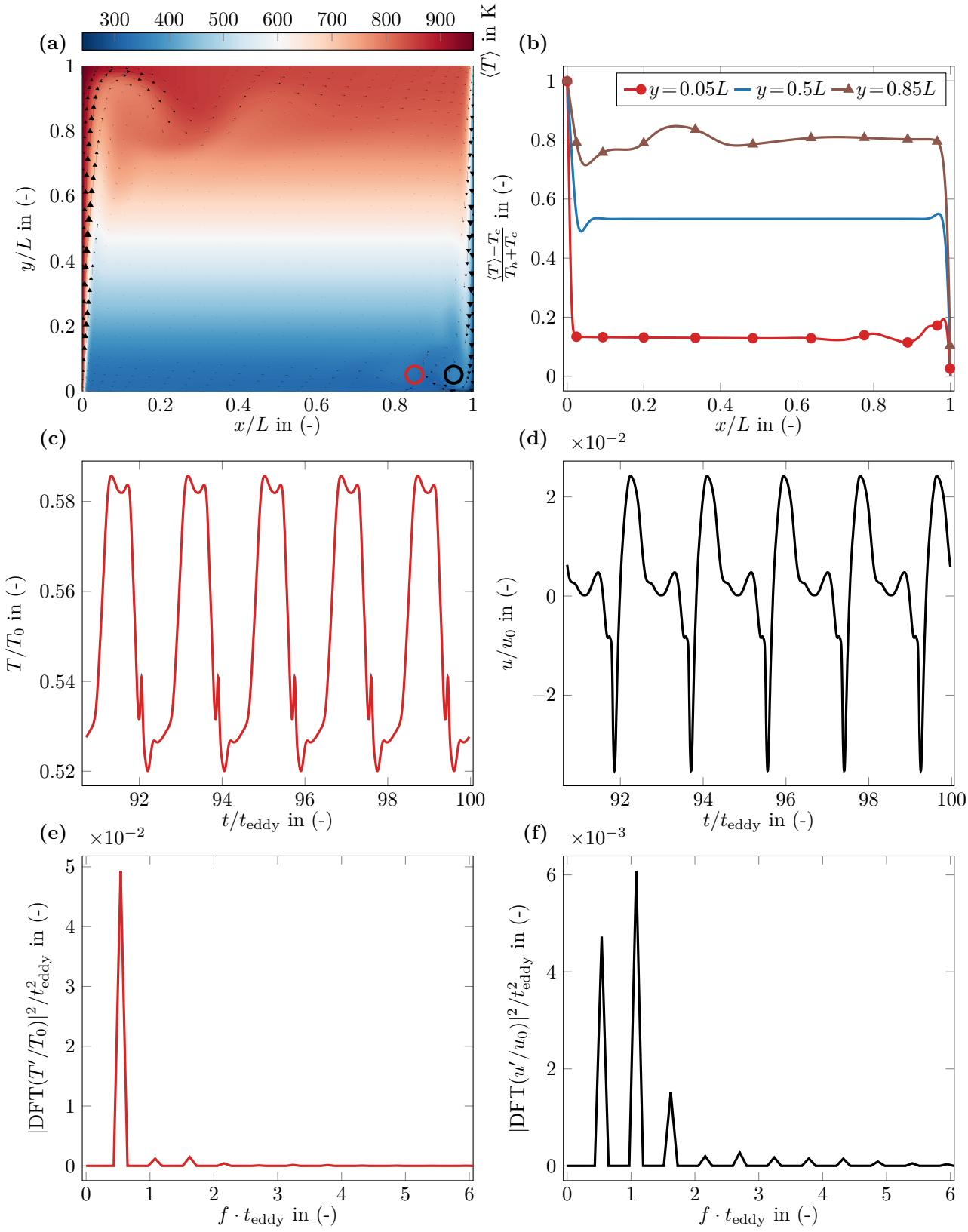

Figure 9: Time averaged temperature $\langle T \rangle$ pseudocolor with velocity vectors field at $t_f = 5.0051 \times 10^3$ s (a) and the corresponding horizontal time-averaged dimensionless temperature profiles at differents vertical positions (b). Time evolution of the instantaneous dimensionless x-velocity $u(x=0.95L, y=0.05L, t)/u_0$ (c) and instantaneous dimensionless temperature $T(x=0.85L, y=0.05L, t)/T_0$ (d) during the last five periods. Power Density Spectrum of the Discret Fourier Transform (DFT) for dimensionless x-velocity fluctuation (e) and temperature fluctuation (f). $\mathrm{CFL_{ac}} = 2.5 \times 10^3$, Chebyshev mesh size 256^2, $t_f = 100 t_{\mathrm{eddy}} = 5.0051 \times 10^3$ s. The probes localisations for (c,d,e,f) plots are drawn on (a).

Mesh	$\langle\overline{\mathrm{Nu}}_{\mathrm{left}}\rangle$	order	$\langle\overline{\mathrm{Nu}}_{\mathrm{left}}\rangle$	order	$\overline{\Delta p}$ in Pa	order
128x128	3.5051×10^{1}	n/a	3.4882×10^{1}	n/a	-6.3892×10^{3}	n/a
256x256	3.4798×10^{1}	n/a	3.4726×10^{1}	n/a	-7.6752×10^{3}	n/a
512x512	3.4739×10^{1}	2.083	3.4689×10^{1}	2.064	-7.9609×10^{3}	2.171
Extrapolation	3.4720×10^{1}	n/a	3.4677×10^{1}	n/a	-8.0425×10^{3}	n/a

Mesh	$\overline{T}$ in K	order	Min Kolmogorov scale in m	order
128x128	6.0788×10^{2}	n/a	2.7653×10^{-1}	n/a
256x256	6.0886×10^{2}	n/a	2.6094×10^{-1}	n/a
512x512	6.0913×10^{2}	1.911	2.5784×10^{-1}	2.328
Extrapolation	6.0922×10^{2}	n/a/	2.5707×10^{-1}	n/a

Table 11: Spatial mesh convergence study of the unsteady compressible natural convection [56]. Time averaged left and right spatially averaged Nusselt values, spatially averaged relative pressure and temperature and the minimal Kolmogorov scale are presented. Chebyshev grid with $\mathrm{CFL}_{\mathrm{ac}} = 2.5\times10^{3}$ and $t_f = 100t_{\mathrm{eddy}}$ s. Extrapolated Richardson's values are also given.

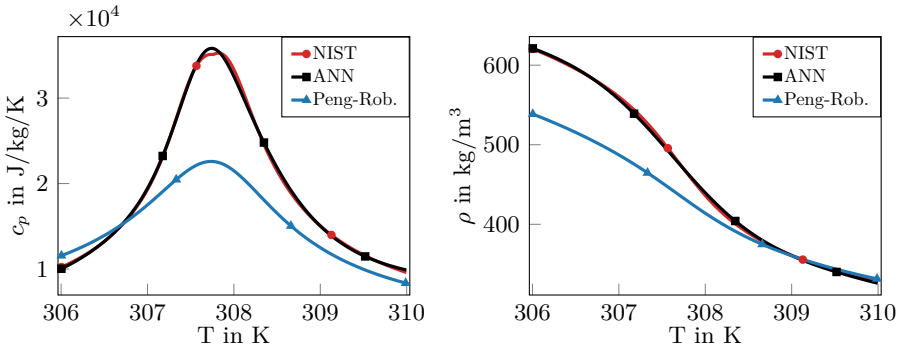

Figure 10: Temperature dependence of specific heat at constant pressure c_p (a) and density (b) at 80 bar. Comparison between Peng–Robinson EoS (blue solid line with triangle symbol), `refprop` NIST (red solid line with circle symbol) and Artifical Neural Network (black solid line with square symbol).

7. Rayleigh–Bénard Direct Numerical Simulation of a supercritical fluid

We finally present an application of IPCMSF for the study of a three-dimensional turbulent subsonic compressible Rayleigh–Bénard flow with a *"real-fluid"* equation of state. The considered thermodynamic point has been chosen to evaluate the very strong materials properties influence on the fluid flow.

Only a few research teams have focused on the study of supercritical fluid flows, often near the critical point and using cubic EoS [63, 64, 65]. The study of turbulence under NOB is beginning to be addressed thanks to DNS numerical experiments either considering water [66] or a supercritical fluid, in the chosen transition zone [67]. Demou and Grigoriadis [66] identified fewer than ten such studies in their bibliography. The present investigation builds upon these efforts and it stands out from previous RB studies that used simpler EoS and considered certain constant properties [63, 64, 65]. We will thus propose advanced numerical simulations from a thermodynamic point of view that will provide a better knowledge of turbulence in these complex fluids where NOB effects seem to predominate [68].

The following section aims to demonstrate the method's ability to handle complex flows by accurately capturing the intricate thermodynamics and turbulent dynamics of a supercritical fluid. The last section shows that the combination of Hypre's library linear system solvers with the Notus CFD code ensures very good scalability on a petascale supercomputer, which is necessary to handle DNS of turbulent flows at high Rayleigh numbers.

7.1. Three-dimensional simulation of supercritical carbon dioxide natural convection

We consider a Rayleigh–Bénard configuration in a three-dimensional cubic cavity of length $L = 3.41\times10^{-3}$ m filled with supercritical carbon dioxide. A vertical temperature difference (ΔT) is im-

posed between the horizontal walls, while the sidewalls are insulated. The top and bottom wall temperatures are respectively cooled and heated ($T_{\text{cold}} = 306$ K and $T_{\text{hot}} = 310$ K). For velocity boundary conditions, no slip conditions are considered. The dimensionless parameters of the case, computed from initial pressure and temperature $(T_0, p_0) = (308\text{ K}, 80\text{ bar})$, are $\text{Ra}_0 = 10^9$, $\text{Ma}_0 = 1.15\times10^{-4}$ (considering the reference velocity $u_0 = \sqrt{\varepsilon L g}$), $\text{Pr}_0 = 1.14\times10^{1}$, $\varepsilon = 1.3\times10^{-2}$.

A complete description of the modelling of the Rayleigh–Bénard turbulent convection problem is beyond the scope of this section. Instead, we focus on the crucial aspect of the accurate calculations of the fluid's thermophysical properties, which strongly depend on temperature and pressure. The chosen modelling considers fully pressure- and temperature-dependent thermophysical properties $x(p, T)$ based on the NIST `refprop` library [62]. Pressure and temperature ranges correspond to a specific thermodynamic area where the fluid properties significantly change (see Figure 10 and notice the ranges of $\beta_p \in [1.89\times10^{-2}, 3.68\times10^{-1}]\text{K}^{-1}$ and $\chi_T \in [5.05\times10^{-8}, 2.21\times10^{-6}]\text{Pa}^{-1}$ in the considered temperature and pressure ranges), mentally delimited by the crossing of the *"Widom Line"* [69]. This *pseudo boiling line* acts as a diffused frontier between gas-like and liquid-like properties of a supercritical fluid, which modify significantly the mass and thermal transport phenomena across this *line*.

The prohibitive computational cost of evaluating all fluid properties using `refprop`, which is not designed for high-performance computing applications, led us to explore the use of Artificial Neural Networks (ANNs) as an efficient alternatives Banuti [70]. These ANNs, trained on `refprop` dataset, are used as EoS and can be viewed as efficient interpolation functions striking a balance between computational efficiency and accurate thermodynamic calculations. The ANN-based method relies on the construction of relatively small neural networks that can represent strong variations in thermodynamic properties (Figure 10), using a unique and easy-to-implement approach. This method eliminates the need for large data tables, which typically require extensive discretization as a function of pressure and temperature to accurately capture steep property gradients. For instance, Rinaldi et al. [71] report the need for 100 grid points per direction, while S. Kawai et al. [72] use a 2D density-pressure grid of 2000×2000 points, claiming it provides a sufficient number of data points at transcritical conditions. The present method uses a neural network with just four neurons in a single hidden layer and a hyperbolic tangent activation function to capture strong property variations. This configuration corresponds to only 37 parameters (weights and biases of the input, hidden, and output layers). Sharing these 37 parameters is significantly more valuable than distributing a large 2D data table for a single material property. The apparent simplicity of the table approach could be reconsidered in light of the widely available machine learning toolkits, which make the ANN-based method straightforward to implement (requiring only matrix-vector operations), even though a detailed CPU time comparison between the different approaches should be adressed.

DNS simulations allow direct access to turbulence without additional modelling and capture phenomena at all scales of the problem, down to the smallest spatial scale, *i.e.* the Batchelor scales in this application where $\text{Pr} > 1$. The flow dynamics are characterized by intense and chaotic bursts of thermal plumes originating from the boundary layers. These plumes interact with the bulk region, driving a dynamic large-scale flow. To accurately capture these phenomena, a uniform mesh is employed, ensuring proper discretization of both the near-wall regions and the bulk. This approach allows for adequate resolution of the plumes as they detach from the boundary layers and penetrate into the bulk zone [64, 73, 68].

We estimated the required mesh size for DNS simulations using the approach outlined by Shishkina et al. [73], which focuses on the boundary layer structure in turbulent convection for incompressible flows. Based on this study, the estimated Kolmogorov and Batchelor space scales were $\eta_K = 2.33\times10^{-5}$ m, $\eta_B = 6.92\times10^{-6}$ m, respectively. Considering a uniform grid, we choose a mesh size of 768^3 (grid size of $\Delta = 4.45\times10^{-6}$ m) with the consideration of a safety factor regarding *a priori* estimations. An *a posteriori* study on the prescribed mesh size allowed to verify the DNS character of the simulation, *i.e.* we compared the minimal and mean values of the Batchelor scale to the grid size: $\Delta = 4.45\times10^{-6}$ m *vs* $\eta_B^{\text{min}} = 3.48\times10^{-6}$ m and $\eta_B^{\text{mean}} = 5.72\times10^{-6}$ m. The numerical schemes are the same as for the other test cases (see Section 4). An adaptative time step based on $\text{CFL}_{\text{ac}} = 4\times10^{3}$ has been imposed which approximatively corresponds along the simulation to $\Delta t = 8\times10^{-5}$s. This range of time step is way smaller than the smallest turbulent timescale, *e.g.* the Kolmogorov and Batchelor timescales are respectively $\tau_{\text{K}} = 5.69\times10^{-3}$ s and $\tau_{\text{B}} = 1.68\times10^{-3}$ s. The simulation until final time took seven job submission of 24 hours on 8,192 cores in the full MPI approach on the Rome partition of TGCC

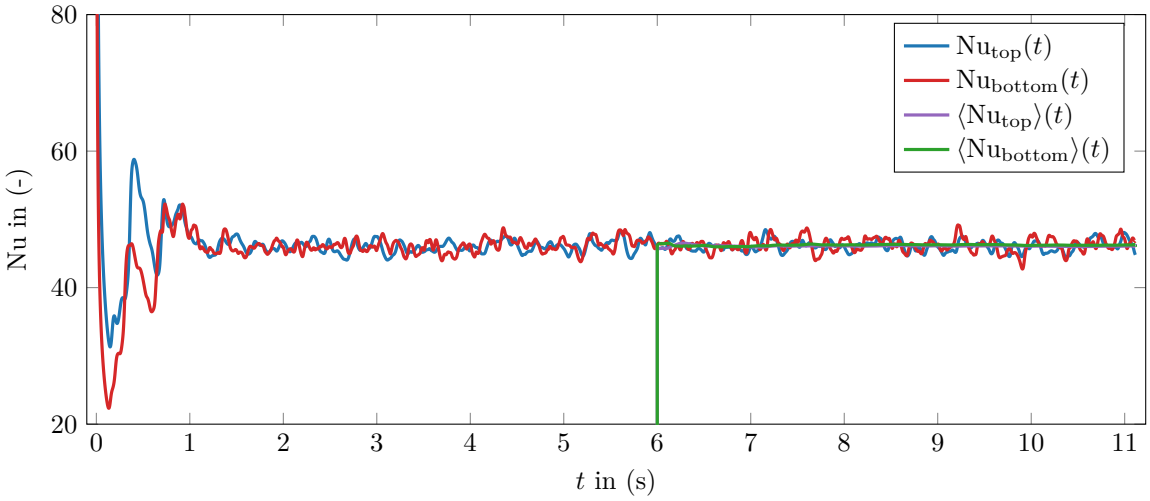

Figure 11: Instantaneous and time averaged evolution of spatially averaged Nusselt numbers on the top and bottom surfaces.

French cluster.

Figure 11 presents the spatially averaged Nusselt numbers of the top and bottom surfaces for both instantaneous and time averaged values, noted $\langle\cdot\rangle$. We identify three phases, starting from the onset of convection ($t \in [0, 0.7]$s), followed by the transitional phase ($t \in [0.7, 2]$s), and finally reaching the fully turbulent regime until the final time $t_f = 11.1$ s, with relative time averaged Nusselt numbers stationnarities below $5{\times}10^{-7}$. The final time averaged spatially averaged Nusselt are respectively for top and bottom $\langle\overline{\mathrm{Nu}}_{\mathrm{top}}\rangle = 4.6262{\times}10^{1}$ and $\langle\overline{\mathrm{Nu}}_{\mathrm{top}}\rangle = 4.6099{\times}10^{1}$. We compared our results with the correlation provided by Demou and Grigoriadis [66] considering NOB effects in a 3D Rayleigh–Bénard cavity filled with water. At $\mathrm{Ra}_0 = 10^9$, their study reported Nusselt numbers of $\mathrm{Nu} = 60.31$ for the 3D case and $\mathrm{Nu} = 50.11$ for the 2D case. In our 3D simulation with supercritical CO_2, the Nusselt number, representing the ratio of total heat transfer to conductive heat transfer, is 23% lower than the 3D result in [66]. Note that water is considered in [66], along with periodic boundary conditions in the y-direction, which enable the use of a FFT solver. For completeness, the 2D version of our case yields a Nusselt number of 38.85, which is 22% lower than the corresponding value in [66].

We present in Figure 12 the instantaneous snapshot of temperature field during the turbulent regime at $t = 4.9$ s. It provides an overview of the flow field structures when turbulent regime is well established within the cavity where detaching plumes from the two top and bottom thermal boundary layers enter the bulk zone viewed with very low opacity.

This section demonstrates the capability of the method to simulate a turbulent Rayleigh–Bénard flow considering highly variable thermophysical properties in a highly compressible fluid. Others simulations will be proposed further to enable an in-depth study of turbulence in fluids with strongly varying properties through a parametric analysis based on the Rayleigh number. Addressing higher Rayleigh number flows in further work, such as $\mathrm{Ra}_0 = 10^{10}$ with a mesh size larger than 1024^3, requires a thorough analysis of the performance and scalability of our IPCMSF implementation to optimize the huge amount of resources allocated to perform this type of simulation.

7.2. Performance and scalability assessments

We conduct in this section a comprehensive performance and parallelization efficiency analysis for the three-dimensional DNS application described in Section 7.1, utilizing the Rome partition of the TGCC French infrastructure for scientific high-performance computing. In this section, we focus on the performance of the code for fully implicit compressible subsonic flow using IPCMSF.

The Notus CFD code's parallel implementation is based on both full MPI and hybrid MPI/OpenMP paradigms. Both implementations were tested on the architecture environment of the Rome partition, which comprises 128 cores per node (AMD Rome@2.6 GHz), 228 GB of RAM per node, and a total of 292,608 cores. In prior work [40] focused on incompressible turbulent flows, communication bottlenecks between MPI processes were identified, and these were mitigated by shifting from a full MPI to the

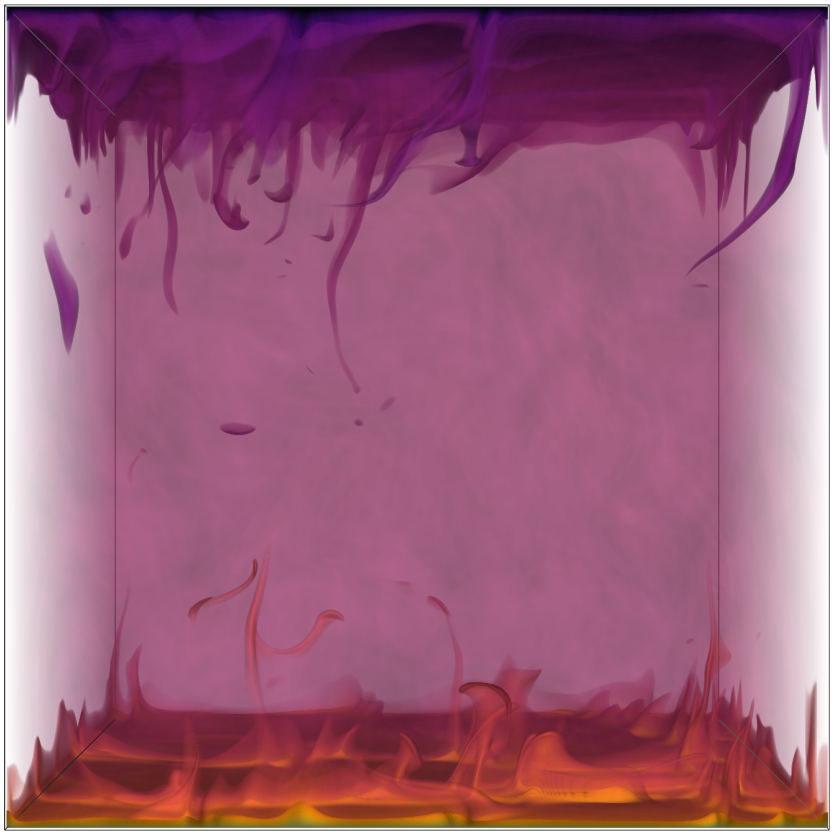

Figure 12: Three-dimensional SLIVR volume rendering of the temperature field (yellow and dark purple respectively stands for 310 K and 306 K) during the turbulent regime at $t = 4.9$s.

	1 thread/process MPI			2 threads/process MPI			4 threads/process MPI			8 threads/process MPI		
	Time/iterations (s)		Efficiency	Time/iterations (s)		Efficiency	Time/iterations (s)		Efficiency	Time/iterations (s)		Efficiency
Core number	Total	Hypre		Total	Hypre		Total	Hypre		Total	Hypre	
8192	8.313	5.521	1.000	7.594	4.809	1.000	8.491	4.898	1.000	14.800	8.581	1.000
16384	6.075	4.224	0.684	5.204	3.401	0.730	5.336	3.217	0.796	8.419	5.260	0.879
32768	6.256	4.618	0.332	4.189	2.746	0.453	3.789	2.441	0.560	4.675	2.730	0.791
65536	8.463	6.592	0.123	5.169	3.608	0.184	4.189	2.636	0.253	4.711	2.970	0.393

Table 12: Strong scalability test with a constant mesh size of $1024^3 \sim 1.07\times10^9$ cells from a full MPI to a hybrid OpenMP/MPI programming paradigm with one, two, four or eight threads per process MPI. Total and Hypre wall clock time spent per iteration are measured. The efficiency is computed considering the total time per iteration. Fully implicit resolution with second-order centered schemes for advection and diffusion, BDF2 temporal scheme.

hybrid OpenMP/MPI approach. The latter allowed us to drastically reduce communication's overhead and improve scalability, particularly for larger numbers of cores up to 131,072 cores.

Given the complexity of performance evaluation across different applications and architecture, as well as the need to explore scalability in terms of both core numbers and problem size (*e.g.*, simulating higher Rayleigh numbers in Rayleigh–Bénard flows), we present strong and weak scalability tests. Tables 12 and 13 compare the performance of full MPI and hybrid MPI/OpenMP approaches, providing the total and Hypre wall clock times per iteration along with the corresponding efficiencies.

Table 12 presents the strong scalability test for a problem size of $1024^3 \sim 1.07\times10^9$ cells. By increasing the number of cores while keeping the constant mesh size, we evaluate the efficiency of workload reduction per core, ideally following Amdahl's law. The initial configuration of 8,192 cores was selected based on prior tests, which showed that 131,072 cells per core yields near-ideal efficiency. For the final configuration of 65,536 cores, the workload is reduced to 16,384 cells per core. In the full MPI implementation, maintaining reasonable efficiency (around 70%) requires a minimum workload of 65,536 cells per core. The hybrid MPI/OpenMP approach, using up to 8 threads per MPI process, significantly enhances performance by reducing communication overhead, particularly at higher core counts. For instance, in the 16,384 core-run, efficiency increased from 0.684 with full MPI to 0.879 with 8 threads per process. This reduction in overhead improves resource utilization, as seen in the 32,768 core simulation, where efficiency rose from 0.331 to 0.791 for this type of mesh size. Thanks to the hybrid paradigm, we improve the strong scalability by reducing communication overhead, especially for large number of cores.

Table 13 shows the weak scalability results considering 40^3 cells per core and goes up to 131,072 cores, corresponding to half of the Rome partition at TGCC. By increasing both the problem size and the core count, we evaluate code performance while maintaining a constant workload of approximately 64,000 cells per core. This workload ensures very good efficiency for both full MPI and hybrid MPI/OpenMP approaches, as shown in Table 12. As the number of cores grows, the problem size increases proportionally, yet the total computation time per iteration only rises slightly due to efficient parallelization. This scalability allows the simulation of significantly larger problems with minimal impact on iteration time. Starting with a mesh size of 8.2 million cells, we scale up to 8.4 billion cells, increasing the problem size by a factor of 1,000. For the 8,192 core-run, we observed an efficiency increase from 0.558 to 0.715 as we shifted from full MPI to the hybrid MPI/OpenMP approach. However, when scaling up further, beyond the 32,768 cores, the efficiency starts to decline. This decrease in efficiency is primarily due to increased communication time as more nodes are added. While the workload per core remains constant, the communication overhead increases and stresses the cluster interconnection technology (latency and limited bandwidth), which limits the scalability. Notably, at 131,072 cores - half of the Rome partition - the efficiency dropped to approximately 0.171 for the full MPI configuration but increased to 0.236 with 2 threads and 0.299 with 4 threads. At this point, the MPI communication time breaks efficiency and suggests that the number 40^3 cells per core should be increase to achieve higher efficiency. These values must be interpreted in the context of the problem size being scaled up by a factor of 1,000. Although the weak efficiency decreases, the ability to simulate a problem 1,000 times larger with a CPU time ratio per time iteration of only 3.3 demonstrates the overall good scalability of the code.

In summary, we have shown that the parallelization approach and proposed numerical methods can handle very large-scale simulations efficiently. The hybrid MPI/OpenMP implementation continues to show improvements, especially in handling communication overhead for large-scale runs. IPCMSF poses no significant challenge for parallel solving using the PFMG preconditioner.

		1 thread/process MPI			2 threads/process MPI			4 threads/process MPI		
		Time/iterations (s)		Efficiency	Time/iterations (s)		Efficiency	Time/iterations (s)		Efficiency
Core number	Mesh size	Total	Hypre		Total	Hypre		Total	Hypre	
128	8.2×10^6	2.795	1.624	1.000	2.732	1.490	1.000	3.260	1.579	1.000
512	3.3×10^7	3.012	1.797	0.928	2.948	1.601	0.927	3.422	1.721	0.953
2048	1.3×10^8	3.402	2.095	0.822	3.266	1.907	0.837	3.654	1.882	0.892
8192	5.2×10^8	5.004	3.415	0.558	4.401	2.735	0.621	4.561	2.561	0.715
32768	2.1×10^9	8.254	5.855	0.339	6.006	3.904	0.455	6.910	4.211	0.472
131072	8.4×10^9	16.300	8.436	0.171	11.560	7.915	0.236	10.910	6.210	0.299

Table 13: Weak scalability test with a constant 40^3 cells per core from a full MPI to a hybrid OpenMP/MPI programming paradigm with one, two and four threads per MPI processes. Total Time per iteration of Total, Notus and Hypre linear system resolution are shown. The efficiency is computed considering the total wall clock time per iteration. Fully implicit resolution with second-order centered schemes for advection and diffusion.

8. Conclusions and perspectives

In this article, we propose an original pressure-based method for compressible flows which solve implicitly an Helmholtz-type equation for the pressure increment variable. This can be sought as a generalization of the incremental pressure correction method of incompressible flows to compressible flows.

The method has been spatially and temporally second-ordered verified, with solutions to flows with Mach number up to 0.6. No significant differences in error magnitudes or second-order temporal convergence were observed, for all the solved fields, when comparing the incremental (IPCMSF) and non-incremental (PCMSF) versions of the algorithm (contrary to what is observed for incompressible flows). The IPCMSF method is validated with both steady and unsteady compressible flows, featuring very large temperature ratio across the domain, thermoacoustic wave propagations in perfect gas as well as very close to the critical point.

The implicit resolution of the pressure field contributes to the increased numerical stability through the utilization of a very large acoustic CFL number whenever the nature of the test case allows for such a large time step, particularly in steady test cases. This results in significant computational time savings. Finally, when fluid properties satisfy the incompressible assumption, the method tends to the incompressible incremental pressure correction method.

The results obtained from the current work thus makes it feasible to advance this approach to more complex scenarios and physical problems such as flows with open and traction boundary conditions in order to avoid reflections at outflow boundaries [74, 75], multiphase flows under the one-fluid compressible Navier-Stokes equations where both phases could exhibit varying different compressibility and be governed by different equation of state, and reactive flows both in open and closed systems. At this point, it should be noted that while the IPCMSF and PCMSF versions of the algorithm do not exhibit significant differences for single-phase compressible problems, in the case of multiphase flow where one of the phases is incompressible, the proposed IPCMSF approach is expected to provide increased precision in that phase, thereby improving global convergence.

Another interesting direction for further investigation would be to transform the Helmholtz-type equation with variable coefficients into a constant-coefficient one involving a Laplacian operator, as proposed for incompressible flows by Dodd and Ferrante [76]. This approach is expected to yield a significant reduction in CPU time and also opens the possibility of using highly efficient FFT-based solvers.

We finally present a DNS of a three-dimensional turbulent Rayleigh–Bénard compressible flow at $Ra = 10^9$ of supercritical carbon dioxide with significant thermophysical properties variations. We also report on this application the performance and scalability results of the implementation of the method, up to 131,072 cores. These results provide new insights into the modelling and simulation of high-pressure and/or high-temperature processes involving complex working fluids such as supercritical CO_2.

9. Acknowledgments

We acknowledge the French National Research Agency for its support, ANR-21-CE01-0018 (ODE-VIE) and ANR-23-1STR-0003 (SINRAM). This study received also financial support from the French

government in the framework of the France 2030 program for University of Bordeaux/RRI BEST (French acronym for Research Network on Factory of the future). Numerical simulations were carried out using the facilities of the MCIA CURTA mesocentre. The Rayleigh–Bénard project was provided with computing HPC and storage resources by GENCI at TGCC thanks to the grant 2023-14621 on the supercomputer Joliot Curie's ROME partition.

Appendix A. Derivation of pressure-energy equation

This section presents the development of the energy conservation expressed in terms of pressure variable. This alternative form of the energy conservation principal is derived by expanding the material derivative of pressure as a function of temperature and density

$$\frac{\mathrm{D}p}{\mathrm{D}t} = \left.\frac{\partial p}{\partial \rho}\right|_T \frac{\mathrm{D}\rho}{\mathrm{D}t} + \left.\frac{\partial p}{\partial T}\right|_\rho \frac{\mathrm{D}T}{\mathrm{D}t}\,, \tag{A.1}$$

with the material derivative of any scalar and vector fields "$*$" being defined as

$$\frac{\mathrm{D}*}{\mathrm{D}t} = \frac{\partial *}{\partial t} + \boldsymbol{v}\cdot\boldsymbol{\nabla} * \,. \tag{A.2}$$

Using mass conservation (1a) and introducing the respective thermodynamic coefficients of isobaric thermal expansion and isothermal compressibility, defined as follows

$$\beta_p = -\frac{1}{\rho}\left.\frac{\partial \rho}{\partial T}\right|_P \quad \text{and} \quad \chi_T = \frac{1}{\rho}\left.\frac{\partial \rho}{\partial p}\right|_T\,, \tag{A.3}$$

equation (A.1) reads

$$\frac{\mathrm{D}p}{\mathrm{D}t} = -\frac{1}{\chi_T}\boldsymbol{\nabla}\cdot\boldsymbol{v} + \frac{\beta_p}{\chi_T}\frac{\mathrm{D}T}{\mathrm{D}t}\,. \tag{A.4}$$

Whether we consider the conservation of energy in c_p formulation (1c) or in c_v formulation,

$$\rho c_v\left(\frac{\partial T}{\partial t} + \boldsymbol{v}\cdot\boldsymbol{\nabla}T\right) = -\frac{T\beta_p}{\chi_T}\boldsymbol{\nabla}\cdot\boldsymbol{v} + \boldsymbol{\nabla}\cdot(\lambda\boldsymbol{\nabla}T) + \Phi_d\,, \tag{A.5}$$

we obtain a unique equation of the conservation of energy expressed in pressure variable. In both cases, after introducing (A.5) or (1c) into equation (A.4) and grouping terms, we get

- in the c_v (A.5) formulation

$$\frac{\mathrm{D}p}{\mathrm{D}t} = -\left(\frac{1}{\chi_T} + \frac{T\beta_p^2}{\rho c_v \chi_T^2}\right)\boldsymbol{\nabla}\cdot\boldsymbol{v} + \frac{\beta_p}{\rho c_v \chi_T}\left(\boldsymbol{\nabla}\cdot(\lambda\boldsymbol{\nabla}T) + \Phi_d\right)\,, \tag{A.6}$$

- in the c_p (1c) formulation

$$\left(1 - \frac{T\beta_p^2}{\rho c_p \chi_T}\right)\frac{\mathrm{D}p}{\mathrm{D}t} = -\frac{1}{\chi_T}\boldsymbol{\nabla}\cdot\boldsymbol{v} + \frac{\beta_p}{\rho c_p \chi_T}\left(\boldsymbol{\nabla}\cdot(\lambda\boldsymbol{\nabla}T) + \Phi_d\right)\,. \tag{A.7}$$

It can be demonstrated that equations (A.6) and (A.7) are identical using several thermodynamic relations, *i.e.* Mayer relation $T\beta_p^2/(\rho c_v \chi_T) = \gamma - 1$, ratios of specific heats $\gamma = c_p/c_v$, definition of the speed of sound $c^2 = 1/(\chi_s \rho)$. These relations allow us to write the following equalities

$$\frac{1}{\chi_T} = \frac{\rho c^2}{\gamma}\,, \quad \frac{T\beta_p^2}{\rho c_v \chi_T} = \gamma - 1 \text{ and } \quad \frac{\beta_p}{\rho c_v \chi_T} = \frac{\beta_p c^2}{c_p}\,. \tag{A.8}$$

Using relations (A.8) in both equations (A.6) and (A.7), we obtain the equation which express the conservation of energy in terms of pressure variable (A.9). The introduced equations do not involve any hypothesis about the considered fluid.

By applying the conservation of energy (1c) in conjunction with thermodynamic relations followed by few algebraic manipulations, we obtain

$$\frac{\mathrm{D}p}{\mathrm{D}t} = -\rho c^2 \boldsymbol{\nabla}\cdot\boldsymbol{v} + \frac{\beta_p c^2}{c_p}\left(\boldsymbol{\nabla}\cdot(\lambda\boldsymbol{\nabla}T) + \Phi_d\right) , \tag{A.9}$$

with c denoting the speed of sound.

The pressure-energy conservation equation for incompressible flow reduces to $\boldsymbol{\nabla}\cdot\boldsymbol{v}=0$ ($c\to\infty$ and $\beta_p=0$), *i.e.* $\mathrm{D}\rho/\mathrm{D}t=0$, which is consistent with the incompressibility limit.

Appendix B. Method of Manufactured Solutions

As discussed earlier in Section 5.3, source terms appear from the method of manufactured solution and they are added in the right-hand side of all resolved equations. In the case of an anisothermal flow without viscous dissipation rate of energy and not subject to gravity, it is necessary to add three source terms for the resolved momentum, energy and pressure equations as

$$\dot{S}_{\boldsymbol{v}} = \rho\frac{D\boldsymbol{v}}{Dt} + \boldsymbol{\nabla}p - \boldsymbol{\nabla}\cdot(\mu\dot{\boldsymbol{\gamma}}) + \frac{2}{3}\boldsymbol{\nabla}\left(\mu\boldsymbol{\nabla}\cdot\boldsymbol{v}\right) , \tag{B.1a}$$

$$\dot{S}_e = \rho c_p\frac{DT}{Dt} - T\beta_p\frac{Dp}{Dt} - \boldsymbol{\nabla}\cdot(\lambda\boldsymbol{\nabla}T) , \tag{B.1b}$$

$$\dot{S}_p = \frac{Dp}{Dt} + \rho c^2\boldsymbol{\nabla}\cdot\boldsymbol{v} - \left(\frac{\beta_p c^2}{c_p}\right)\left(\boldsymbol{\nabla}\cdot(\lambda\boldsymbol{\nabla}T) + \dot{S}_e\right) . \tag{B.1c}$$

As we do not solve energy considering isothermal flow, we only compute two source terms for momentum and pressure equations. The isothermal pressure source term reads

$$\dot{S}_p = \frac{Dp}{Dt} + \rho c^2\boldsymbol{\nabla}\cdot\boldsymbol{v} . \tag{B.2}$$

As we consider a perfect gas in Section 5.3, the time- and space-dependent thermodynamic properties of the fluid are computed as $\rho=p/RT$, $\chi_T=1/p$, $\beta_p=1/T$ and $c^2=\gamma p/\rho$.

For the sake of reproducibility, the source terms of the isothermal manufactured solution (see Section 5.3.1) is given below. They are the result of the differentiation of equations (B.1a) and (B.2) The momentum and pressure source terms read respectively

$$\begin{aligned}
\dot{S}_{\boldsymbol{v}_x} =& 4\pi^2\mu u_0\cos(2\pi ft)\ \big\{\sin^2(\pi x)\sin(2\pi y) - \sin(2\pi y)\cos^2(\pi x) \\
&\qquad + \sin^2(\pi x)\sin(2\pi y) - \sin(\pi y)\cos(2\pi x)\cos(\pi y)\big\} \\
&+ \frac{2\mu}{3}u_0\cos(2\pi ft)\left\{2\pi^2\sin(2\pi y)\cos^2(\pi x) - 2\pi^2\sin^2(\pi x)\sin(2\pi y)\right. \\
&\qquad \left. + 4\pi^2\sin(\pi y)\cos(2\pi x)\cos(\pi y)\right\} \\
&+ p_1\pi\cos(2\pi ft)\ \cos(\pi x)\sin(\pi y) \\
&+ 2\pi u_0\frac{p(x,y,t)}{T_0 R}\ \big\{-f\sin^2(\pi x)\sin(2\pi y)\sin(2\pi ft) \\
&\qquad + u_0\sin^3(\pi x)\sin^2(2\pi y)\cos(\pi x)\cos^2(2\pi ft) \\
&\qquad + u_0\sin^2(\pi x)\sin(2\pi x)\sin^2(\pi y)\cos(2\pi y)\cos^2(2\pi ft)\big\} ,
\end{aligned} \tag{B.3}$$

$$\begin{aligned}
\dot{S}_{\boldsymbol{v}_y} =& 4\pi^2\mu u_0\cos(2\pi ft)\ \big\{\sin(2\pi x)\sin^2(\pi y) - \sin(2\pi x)\cos^2(\pi y) \\
&\qquad - \sin(\pi x)\cos(\pi x)\cos(2\pi y) + \sin(2\pi x)\sin^2(\pi y)\big\} \\
&+ \frac{2\mu}{3}u_0\cos(2\pi ft)\left\{2\pi^2\sin(2\pi x)\cos^2(\pi y) - 2\pi^2\sin(2\pi x)\sin^2(\pi y)\right. \\
&\qquad \left. + 4\pi^2\sin(\pi x)\cos(\pi x)\cos(2\pi y)\right\} \\
&+ p_1\pi\cos(2\pi ft)\ \cos(\pi y)\sin(\pi x) \\
&+ 2\pi u_0\frac{p(x,y,t)}{T_0 R}\ \big\{-f\sin(2\pi x)\sin^2(\pi y)\sin(2\pi ft) \\
&\qquad + u_0\sin^3(\pi y)\sin^2(2\pi x)\cos(\pi y)\cos^2(2\pi ft) \\
&\qquad + u_0\sin^2(\pi x)\sin^2(\pi y)\sin(2\pi y)\cos(2\pi x)\cos^2(2\pi ft)\big\} ,
\end{aligned} \tag{B.4}$$

Test-case	T^* in K	μ^* in Pa s	λ^* in W m^{-1} K^{-1}
Le Quéré et al. [10] case T2	273	1.68×10^{-5}	2.38×10^{-2}
Bouafia and Daube [55]	300	1.68×10^{-5}	2.38×10^{-2}
Wen et al. [56]	273	2.96×10^{2}	2.30×10^{-1}

Table C.14: Values of the parameters of Sutherland's law for the proposed test cases. All test cases have the same $S=110.5$.

$$\begin{aligned}\dot{S}_p =&\pi p_1 u_0 \cos^2(2\pi f t)\left\{\sin^2(\pi x)\sin(\pi y)\sin(2\pi y)\cos(\pi x)+\sin(\pi x)\sin(2\pi x)\sin^2(\pi y)\cos(\pi y)\right\} \\ &+\gamma 2\pi u_0 p(x,y,t)\cos(2\pi f t)\left\{\sin(\pi x)\sin(2\pi y)\cos(\pi x)+\sin(2\pi x)\sin(\pi y)\cos(\pi y)\right\} \\ &-2\pi f p_1 \sin(\pi x)\sin(\pi y)\sin(2\pi f t)\,.\end{aligned} \tag{B.5}$$

Sources terms have been computed using the symbolic computing `python` module `sympy`. Due to the long analytical expressions of the source terms for the anisothermal manufactured solution (see Section 5.3.2), we do not include them in the appendix. We refer the reader to the initialization file of each test case available in the Notus CFD repository [39].

Appendix C. Parameter values of material laws

For the sake of easily reproducible verification and validation process, we present in Table C.14 the values of Sutherland's law parameters used in our test cases. We recall Sutherland's law for a material properties x

$$x(T) = x^*\frac{T^*+S}{T+S}\left(\frac{T}{T^*}\right)^{3/2}, \tag{C.1}$$

with x^*, T^* and S the three parameters of the law.

The viscosity and conductivity law of the thermoacoustic wave propagation of Huang and Bau [57] has been set by a quartic temperature law polynomial. Material properties x is thus computed as

$$x(T) = \sum_{i=0}^{3} a_{xi}T^i\,, \tag{C.2}$$

with a_{xi} the i^{th} constant parameter in $[x]\text{K}^{-i}$ with $[x]$ the unit of x. We set for viscosity and conductivity respectively

$$(a_{\mu 0}, a_{\mu 1}, a_{\mu 2}, a_{\mu 3}) = (1.24\times10^{-6}, 6.32\times10^{-8}, -4.65\times10^{-11}, 2.01\times10^{-14})\,, \tag{C.3}$$

$$(a_{\lambda 0}, a_{\lambda 1}, a_{\lambda 2}, a_{\lambda 3}) = (-7.26\times10^{-4}, 9.76\times10^{-5}, -7.18\times10^{-8}, 3.10\times10^{-11})\,. \tag{C.4}$$

Appendix D. Temporal convergence results of the verification part for the pressure correction method for compressible flows

Δt in s	$\|\|\varepsilon_p\|\|_{L_2}$	order	$\|\|\varepsilon_p\|\|_{L_\infty}$	order	$\|\|\varepsilon_T\|\|_{L_2}$	order
4.00×10^{-4}	1.381×10^{-2}	n/a	1.381×10^{1}	n/a	2.381×10^{-7}	n/a
2.00×10^{-4}	3.405×10^{-3}	2.020	3.405	2.020	7.652×10^{-8}	1.638
1.00×10^{-4}	8.381×10^{-4}	2.022	8.382×10^{-1}	2.022	2.351×10^{-8}	1.703
5.00×10^{-5}	1.966×10^{-4}	2.092	1.967×10^{-1}	2.092	9.949×10^{-9}	1.240
2.50×10^{-5}	5.342×10^{-5}	1.879	5.352×10^{-2}	1.877	1.156×10^{-9}	3.106
1.25×10^{-5}	1.304×10^{-5}	2.035	1.314×10^{-2}	2.026	3.850×10^{-10}	1.586

Δt in s	$\|\|\varepsilon_T\|\|_{L_\infty}$	order	$\|\|\varepsilon_\rho\|\|_{L_2}$	order	$\|\|\varepsilon_\rho\|\|_{L_\infty}$	order
4.00×10^{-4}	2.382×10^{-4}	n/a	1.092×10^{-7}	n/a	1.092×10^{-4}	n/a
2.00×10^{-4}	7.652×10^{-5}	1.638	2.705×10^{-8}	2.013	2.705×10^{-5}	2.013
1.00×10^{-4}	2.351×10^{-5}	1.703	6.693×10^{-9}	2.015	6.694×10^{-6}	2.015
5.00×10^{-5}	9.955×10^{-6}	1.240	1.601×10^{-9}	2.063	1.602×10^{-6}	2.063
2.50×10^{-5}	1.162×10^{-6}	3.099	4.242×10^{-10}	1.917	4.250×10^{-7}	1.915
1.25×10^{-5}	3.912×10^{-7}	1.570	1.043×10^{-10}	2.024	1.051×10^{-7}	2.015

Table D.15: PCMSF temporal order accuracy of the isentropic injection test case. First time step $\Delta t = 4\times10^{-4}$ s equal to $\mathrm{CFL_{ac}} = 1.78\times10^{4}$. Mesh size 128^2, $t_f = 1\times10^{-1}$ s.

Δt in s	$\|\|\varepsilon_v\|\|_{L_2}$	order	$\|\|\varepsilon_v\|\|_{L_\infty}$	order	$\|\|\varepsilon_p\|\|_{L_2}$	order
2.00×10^{-4}	3.840×10^{1}	n/a	6.169×10^{1}	n/a	5.521×10^{3}	n/a
1.00×10^{-4}	1.478×10^{1}	1.377	2.524×10^{1}	1.289	1.845×10^{3}	1.581
5.00×10^{-5}	4.260	1.795	7.839	1.687	5.349×10^{2}	1.786
2.50×10^{-5}	1.114	1.935	2.099	1.901	1.405×10^{2}	1.929
1.25×10^{-5}	2.863×10^{-1}	1.960	5.454×10^{-1}	1.944	3.582×10^{1}	1.971
6.25×10^{-6}	7.666×10^{-2}	1.901	1.469×10^{-1}	1.892	9.573	1.904

Δt in s	$\|\|\varepsilon_p\|\|_{L_\infty}$	order	$\|\|\varepsilon_\rho\|\|_{L_2}$	order	$\|\|\varepsilon_\rho\|\|_{L_\infty}$	order
2.00×10^{-4}	1.373×10^{4}	n/a	6.412×10^{-2}	n/a	1.595×10^{-1}	n/a
1.00×10^{-4}	5.012×10^{3}	1.454	2.143×10^{-2}	1.581	5.821×10^{-2}	1.454
5.00×10^{-5}	1.646×10^{3}	1.607	6.212×10^{-3}	1.786	1.912×10^{-2}	1.607
2.50×10^{-5}	4.416×10^{2}	1.898	1.632×10^{-3}	1.929	5.129×10^{-3}	1.898
1.25×10^{-5}	1.131×10^{2}	1.965	4.161×10^{-4}	1.971	1.314×10^{-3}	1.965
6.25×10^{-6}	2.988×10^{1}	1.921	1.112×10^{-4}	1.904	3.470×10^{-4}	1.921

Table D.16: PCMSF temporal order accuracy of the isothermal high Mach manufactured solution. First time step $\Delta t = 2\times10^{-4}$ s equal to $\mathrm{CFL_{ac}} = 1.78\times10^{1}$. Mesh size 256^2 and $t_f = 2\times10^{-3}$ s.

Δt in s	$\|\|\varepsilon_v\|\|_{L_2}$	order	$\|\|\varepsilon_v\|\|_{L_\infty}$	order	$\|\|\varepsilon_p\|\|_{L_2}$	order	$\|\|\varepsilon_p\|\|_{L_\infty}$	order
2.00×10^{-4}	3.671×10^{1}	n/a	7.153×10^{1}	n/a	5.846×10^{3}	n/a	1.905×10^{4}	n/a
1.00×10^{-4}	1.354×10^{1}	1.439	2.449×10^{1}	1.546	1.866×10^{3}	1.648	5.326×10^{3}	1.839
5.00×10^{-5}	3.857	1.811	6.855	1.837	5.199×10^{2}	1.844	1.555×10^{3}	1.776
2.50×10^{-5}	1.008	1.935	1.834	1.902	1.349×10^{2}	1.946	4.046×10^{2}	1.943
1.25×10^{-5}	2.587×10^{-1}	1.963	4.769×10^{-1}	1.944	3.414×10^{1}	1.982	1.057×10^{2}	1.936
6.25×10^{-6}	6.857×10^{-2}	1.916	1.294×10^{-1}	1.882	8.946	1.932	2.825×10^{1}	1.904

Δt in s	$\|\|\varepsilon_T\|\|_{L_2}$	order	$\|\|\varepsilon_T\|\|_{L_\infty}$	order	$\|\|\varepsilon_\rho\|\|_{L_2}$	order	$\|\|\varepsilon_\rho\|\|_{L_\infty}$	order
2.00×10^{-4}	6.862	n/a	3.303×10^{1}	n/a	5.182×10^{-2}	n/a	1.888×10^{-1}	n/a
1.00×10^{-4}	2.478	1.469	8.697	1.925	1.705×10^{-2}	1.603	4.490×10^{-2}	2.072
5.00×10^{-5}	6.791×10^{-1}	1.868	2.413	1.850	4.738×10^{-3}	1.848	1.406×10^{-2}	1.675
2.50×10^{-5}	1.760×10^{-1}	1.948	6.314×10^{-1}	1.934	1.233×10^{-3}	1.942	4.035×10^{-3}	1.801
1.25×10^{-5}	4.506×10^{-2}	1.965	1.616×10^{-1}	1.967	3.142×10^{-4}	1.973	1.067×10^{-3}	1.919
6.25×10^{-6}	1.214×10^{-2}	1.892	4.273×10^{-2}	1.919	8.324×10^{-5}	1.916	2.858×10^{-4}	1.900

Table D.17: PCMSF temporal order accuracy of the anisothermal high Mach subsonic manufactured solution. First time step $\Delta t = 2\times10^{-4}$ s equal to $\mathrm{CFL_{ac}} = 1.78\times10^{1}$. Mesh size 256^2 and $t_f = 2\times10^{-3}$ s.

Δt in s	$\|\|\varepsilon_v\|\|_{L_2}$	order	$\|\|\varepsilon_v\|\|_{L_\infty}$	order	$\|\|\varepsilon_p\|\|_{L_2}$	order	$\|\|\varepsilon_p\|\|_{L_\infty}$	order
2.00×10^{-4}	3.7293×10^{-1}	n/a	8.8203×10^{-1}	n/a	2.1545×10^{2}	n/a	4.5007×10^{2}	n/a
1.00×10^{-4}	1.3905×10^{-1}	1.4230	3.1777×10^{-1}	1.4730	6.5280×10^{1}	1.7230	1.5497×10^{2}	1.5380
5.00×10^{-5}	4.1078×10^{-2}	1.7590	9.1070×10^{-2}	1.8030	1.8298×10^{1}	1.8350	5.2502×10^{1}	1.5620
2.50×10^{-5}	1.0988×10^{-2}	1.9020	2.3610×10^{-2}	1.9480	4.7298	1.9520	1.4277×10^{1}	1.8790
1.25×10^{-5}	2.8200×10^{-3}	1.9620	6.0093×10^{-3}	1.9740	1.1912	1.9890	3.6296	1.9760
6.25×10^{-6}	7.1785×10^{-4}	1.9740	1.5043×10^{-3}	1.9980	2.9928×10^{-1}	1.9930	9.1812×10^{-1}	1.9830

Δt in s	$\|\|\varepsilon_T\|\|_{L_2}$	order	$\|\|\varepsilon_T\|\|_{L_\infty}$	order	$\|\|\varepsilon_\rho\|\|_{L_2}$	order	$\|\|\varepsilon_\rho\|\|_{L_\infty}$	order
2.00×10^{-4}	4.1657	n/a	1.3491×10^{1}	n/a	1.8571×10^{-2}	n/a	6.5706×10^{-2}	n/a
1.00×10^{-4}	8.7463×10^{-1}	2.2520	2.4994	2.4320	3.7121×10^{-3}	2.3230	1.1901×10^{-2}	2.4650
5.00×10^{-5}	1.9027×10^{-1}	2.2010	4.3358×10^{-1}	2.5270	7.8204×10^{-4}	2.2470	2.0998×10^{-3}	2.5030
2.50×10^{-5}	4.5704×10^{-2}	2.0580	1.1716×10^{-1}	1.8880	1.8187×10^{-4}	2.1040	5.1266×10^{-4}	2.0340
1.25×10^{-5}	1.1398×10^{-2}	2.0040	3.1931×10^{-2}	1.8750	4.4410×10^{-5}	2.0340	1.3708×10^{-4}	1.9030
6.25×10^{-6}	2.8613×10^{-3}	1.9940	8.3194×10^{-3}	1.9400	1.1023×10^{-5}	2.0100	3.5404×10^{-5}	1.9530

Table D.18: PCMSF temporal order accuracy of the anisothermal low Mach manufactured solution. First time step $\Delta t = 2\times10^{-4}$ s equal to $\mathrm{CFL_{ac}} = 1.78\times10^{1}$. Mesh size 256^2 and $t_f = 2\times10^{-3}$ s.

References

[1] S. K. Godunov and I. O. Bohachevsky. Finite difference method for numerical computation of discontinuous solutions of the equations of fluid dynamics. 1959. URL https://api.semanticscholar.org/CorpusID:126255486.

[2] P.L. Roe. Approximate riemann solvers, parameter vectors, and difference schemes. *Journal of Computational Physics*, 43(2):357–372, 1981. doi: 10.1016/0021-9991(81)90128-5. URL https://doi.org/10.1016/0021-9991(81)90128-5.

[3] R.W. Maccormack. A numerical method for solving the equations of compressible viscous flow. *AIAA Journal*, 20:1275–1281, 1981. URL https://api.semanticscholar.org/CorpusID:209843221.

[4] E. Turkel. Preconditioned methods for solving the incompressible and low speed compressible equations. *Journal of Computational Physics*, 72(2):277–298, 1987. doi: 10.1016/0021-9991(87)90084-2. URL https://doi.org/10.1016/0021-9991(87)90084-2.

[5] M. Pelanti. Low mach number preconditioning techniques for roe-type and hllc-type methods for a two-phase compressible flow model. *Applied Mathematics and Computation*, 310:112–133, 2017. doi: 10.1016/j.amc.2017.04.014. URL https://doi.org/10.1016/j.amc.2017.04.014.

[6] A. J. Chorin. A numerical method for solving incompressible viscous flow problems. *Journal of Computational Physics*, 2(1):12–26, 1967. doi: 10.1016/0021-9991(67)90037-x.

[7] S.V. Patankar. *Numerical heat transfer and fluid flow*. Series on Computational Methods in Mechanics and Thermal Science. Hemisphere Publishing Corporation (CRC Press, Taylor & Francis Group), 1980. URL http://www.crcpress.com/product/isbn/9780891165224.

[8] S. Paolucci. On the filtering of sound from the Navier–Stokes equations. *NASA STI/Recon Technical Report N*, 83:26036, 1982.

[9] C. Wall, C. D. Pierce, and P. Moin. A semi-implicit method for resolution of acoustic waves in low mach number flows. *Journal of Computational Physics*, 181(2):545–563, 2002. doi: 10.1006/jcph.2002.7141.

[10] P. Le Quéré, C. Weisman, H. Paillère, J. Vierendeels, E. Dick, R. Becker, M. Braack, and J. Locke. Modelling of natural convection flows with large temperature differences: A benchmark problem for low mach number solvers. part 1. reference solutions. *ESAIM: Mathematical Modelling and Numerical Analysis*, 39(3):609–616, 2005. doi: 10.1051/m2an:2005027.

[11] V. Daru, P. Le Qéré, M.-C. Duluc, and O. Le Maître. A numerical method for the simulation of low mach number liquid-gas flows. *Journal of Computational Physics*, 229(23):8844–8867, 2010. doi: 10.1016/j.jcp.2010.08.013. URL https://doi.org/10.1016/j.jcp.2010.08.013.

[12] A. Bermúdez, S. Busto, M. Dumbser, J.L. Ferrín, L. Saavedra, and M.E. Vázquez-Cendón. A staggered semi-implicit hybrid FV/FE projection method for weakly compressible flows. *Journal of Computational Physics*, 421:109743, 2020. doi: 10.1016/j.jcp.2020.109743. URL https://doi.org/10.1016/j.jcp.2020.109743.

[13] A. Hennink, M. Tiberga, and D. Lathouwers. A pressure-based solver for low-mach number flow using a discontinuous galerkin method. *Journal of Computational Physics*, 425:109877, 2021. doi: 10.1016/j.jcp.2020.109877. URL http://dx.doi.org/10.1016/j.jcp.2020.109877.

[14] Y. Cang and L. Wang. An improved fractional-step method on co-located unstructured meshes for weakly compressible flow simulations. *Computers and Fluids*, 253, 2023. doi: 10.1016/j.compfluid.2022.105775.

[15] T. Yabe and P.Y. Wang. Unified numerical procedure for compressibleand incompressible fluid. *Journal of the Physical Society of Japan*, 60(7):2105–2108, 1991. doi: 10.1143/JPSJ.60.2105. URL https://doi.org/10.1143/JPSJ.60.2105.

[16] F. Moukalled and M. Darwish. A unified formulation of the segregated class of algorithms for fluid flow at all speeds. *Numerical Heat Transfer, Part B: Fundamentals*, 37(1):103–139, 2000. doi: 10.1080/104077900275576.

[17] F. Xiao, R. Akoh, and S. Ii. Unified formulation for compressible and incompressible flows by using multi-integrated moments II: multi-dimensional version for compressible and incompressible flows. *Journal of Computational Physics*, 213(1):31–56, 2006. doi: 10.1016/j.jcp.2005.08.002. URL https://doi.org/10.1016/j.jcp.2005.08.002.

[18] D. Fuster and S. Popinet. An all-mach method for the simulation of bubble dynamics problems in the presence of surface tension. *Journal of Computational Physics*, 374:752–768, 2018. doi: 10.1016/j.jcp.2018.07.055. URL https://doi.org/10.1016/j.jcp.2018.07.055.

[19] R.I. Issa, A.D. Gosman, and A.P. Watkins. Solution of the implicitly discretized fluid flow equation by operator splitting. *Journal of Computational Physics*, 62:40–65, 1986.

[20] K. Goda. A multistep technique with implicit difference schemes for calculating two- or three-dimensional cavity flows. *Journal of Computational Physics*, 30(1):76–95, 1979. doi: 10.1016/0021-9991(79)90088-3.

[21] L. J. P. Timmermans, P. D. Minev, and F. N. Van de Vosse. An approximate projection scheme for incompressible flow using spectral elements. *International Journal for Numerical Methods in Fluids*, 22(7):673–688, 1996. doi: 10.1002/(sici)1097-0363(19960415)22:7<673::aid-fld373>3.0.co;2-o.

[22] J.L. Guermond, P. Minev, and Jie Shen. An overview of projection methods for incompressible flows. *Computer Methods in Applied Mechanics and Engineering*, 195(44-47):6011–6045, 2006. doi: 10.1016/j.cma.2005.10.010.

[23] N. Kwatra, J. Su, J.T. Grétarsson, and R. Fedkiw. A method for avoiding the acoustic time step restriction in compressible flow. *Journal of Computational Physics*, 228(11):4146–4161, 2009. doi: 10.1016/j.jcp.2009.02.027. URL https://doi.org/10.1016/j.jcp.2009.02.027.

[24] J. M. Vedovoto, A. da Silveira Neto, A. Mura, and L.F. Figueira da Silva. Application of the method of manufactured solutions to the verification of a pressure-based finite-volume numerical scheme. *Computers & Fluids*, 51(1):85–99, 2011. doi: 10.1016/j.compfluid.2011.07.014. URL https://doi.org/10.1016/j.compfluid.2011.07.014.

[25] A. Urbano, M. Bibal, and S. Tanguy. A semi implicit compressible solver for two-phase flows of real fluids. *Journal of Computational Physics*, 456:111034, 2022. doi: 10.1016/j.jcp.2022.111034.

[26] A.D. Demou, N. Scapin, M. Pelanti, and L. Brandt. A pressure-based diffuse interface method for low-mach multiphase flows with mass transfer. *Journal of Computational Physics*, 448:110730, 2022. doi: 10.1016/j.jcp.2021.110730. URL https://doi.org/10.1016/j.jcp.2021.110730.

[27] V. Moureau, C. Bérat, and H. Pitsch. An efficient semi-implicit compressible solver for large-eddy simulations. *Journal of Computational Physics*, 226(2):1256–1270, 2007. doi: 10.1016/j.jcp.2007.05.035. URL https://doi.org/10.1016/j.jcp.2007.05.035.

[28] G. Reichling, B. Noll, and M. Aigner. Development of a projection-based method for the numerical calculation of compressible reactive flows. In *51st AIAA Aerospace Sciences Meeting including the New Horizons Forum and Aerospace Exposition*. American Institute of Aeronautics and Astronautics, 2013. doi: 10.2514/6.2013-1003.

[29] C. J. Roy, C. C. Nelson, T. M. Smith, and C. C. Ober. Verification of Euler/Navier–Stokes codes using the method of manufactured solutions. *International Journal for Numerical Methods in Fluids*, 44(6):599–620, February 2004. doi: 10.1002/fld.660.

[30] C. Bayona, J. Baiges, and R. Codina. Solution of low mach number aeroacoustic flows using a variational multi-scale finite element formulation of the compressible Navier–Stokes equations written in primitive variables. *Computer Methods in Applied Mechanics and Engineering*, 344:1073–1103, 2019. doi: 10.1016/j.cma.2018.01.040.

[31] F. Navah. *Development, Verification and Validation of High-Order Methods for the Simulation of Turbulence*. Phd thesis, McGill University, 2019.

[32] A. Toutant. General and exact pressure evolution equation. *Physics Letters A*, 381(44):3739–3742, nov 2017. doi: 10.1016/j.physleta.2017.10.008.

[33] S. Y. Yoon and T. Yabe. The unified simulation for incompressible and compressible flow by the predictor-corrector scheme based on the CIP method. *Computer Physics Communications*, 119 (2-3):149–158, 1999. doi: 10.1016/s0010-4655(99)00192-7.

[34] J.-P. Caltagirone, S. Vincent, and C. Caruyer. A multiphase compressible model for the simulation of multiphase flows. *Computers & Fluids*, 50(1):24–34, 2011. doi: 10.1016/j.compfluid.2011.06.011.

[35] H. Terashima and M. Koshi. Approach for simulating gas–liquid-like flows under supercritical pressures using a high-order central differencing scheme. *Journal of Computational Physics*, 231 (20):6907–6923, 2012. doi: 10.1016/j.jcp.2012.06.021.

[36] S. Amiroudine, J.-P. Caltagirone, and A. Erriguible. A lagrangian–eulerian compressible model for the trans-critical path of near-critical fluids. *International Journal of Multiphase Flow*, 59: 15–23, 2014. doi: doi.org/10.1016/j.ijmultiphaseflow.2013.10.008.

[37] Y. Saade, D. Lohse, and D. Fuster. A multigrid solver for the coupled pressure-temperature equations in an all-mach solver with VoF. *Journal of Computational Physics*, 476:111865, 2023. doi: 10.1016/j.jcp.2022.111865.

[38] K. Khadra, P. Angot, S. Parneix, and J.-P. Caltagirone. Fictitious domain approach for numerical modelling of Navier–Stokes equations. *International Journal for Numerical Methods in Fluids*, 34 (8):651–684, 2000.

[39] Notus computational fluid dynamics, v0.6.0. [https://notus-cfd.org/], 2024.

[40] S. Glockner, A. M. D. Jost, and A. Erriguible. Advanced petascale simulations of the scaling up of mixing limited flow processes for materials synthesis. *Chemical Engineering Journal*, 431(Part 1):133647 (9 p.), 2022. doi: 10.1016/j.cej.2021.133647.

[41] A.H. Baker, R.D. Falgout, T.V. Kolev, and U.M. Yang. *Scaling Hypre's Multigrid Solvers to 100,000 Cores*, pages 261–279. 2012. doi: 10.1007/978-1-4471-2437-5_13.

[42] D. Sharma, M. Coquerelle, A. Erriguible, and S. Amiroudine. Adaptive interface thickness based mobility-phase-field method for incompressible fluids. *International Journal of Multiphase Flow*, 142:103687, 2021. doi: 10.1016/j.ijmultiphaseflow.2021.103687.

[43] A.M.D. Jost and S. Glockner. Direct forcing immersed boundary methods: Improvements to the ghost-cell method. *Journal of Computational Physics*, 438:110371, 2021. doi: 10.1016/j.jcp.2021.110371. URL https://doi.org/10.1016/j.jcp.2021.110371.

[44] A.M.D. Jost, S. Glockner, and A. Erriguible. Direct numerical simulations of fluids mixing above mixture critical point. *The Journal of Supercritical Fluids*, 165:104939, 2020. doi: 10.1016/j.supflu.2020.104939. URL https://www.sciencedirect.com/science/article/pii/S089684462030190X.

[45] A. Lemoine, S. Glockner, and J. Breil. Moment-of-fluid analytic reconstruction on 2D cartesian grids. *Journal of Computational Physics*, 328:131–139, 2017. doi: 10.1016/j.jcp.2016.10.013. URL https://doi.org/10.1016/j.jcp.2016.10.013.

[46] M. Coquerelle and S. Glockner. A fourth-order accurate curvature computation in a level set framework for two-phase flows subjected to surface tension forces. *Journal of Computational Physics*, 305:838–876, 2016. doi: 10.1016/j.jcp.2015.11.014.

[47] W. Oberkampf and T. Trucano. *Verification and Validation in Computational Fluid Dynamics*. 2002. doi: 10.2172/793406.

[48] C. J. Roy. Review of code and solution verification procedures for computational simulation. *Journal of Computational Physics*, 205(1):131–156, 2005. doi: 10.1016/j.jcp.2004.10.036.

[49] P.J. Roache. *Verification and Validation in Computational Science and Engineering*. Hermosa Publishers, 1998. URL https://books.google.fr/books?id=ENRlQgAACAAJ.

[50] J.-P. Caltagirone. An alternative model of euler equations based on conservation of acceleration. *Submited to Journal of Computational Physics*, 2024.

[51] L. Shunn, F. Ham, P. Knupp, and P. Moin. Verification of low-mach number combustion codes using the method of manufactured solutions. *CSRI Summer Proceedings*, pages 126–36, 2007.

[52] P. Le Quéré. Accurate solutions to the square thermally driven cavity at high Rayleigh number. *Computers & Fluids*, 20(1):29–41, 1991. doi: 10.1016/0045-7930(91)90025-d.

[53] J. Vierendeels, B. Merci, and E. Dick. Benchmark solutions for the natural convective heat transfer problem in a square cavity with large horizontal temperature differences. *International Journal of Numerical Methods for Heat & Fluid Flow*, 13(8):1057–1078, 2003. doi: 10.1108/09615530310501957.

[54] T. W. I. Kuan and J. Szmelter. A numerical framework for low-speed flows with large thermal variations. *Computers & Fluids*, 265:105989, 2023. doi: 10.1016/j.compfluid.2023.105989. URL https://doi.org/10.1016/j.compfluid.2023.105989.

[55] M. Bouafia and O. Daube. Natural convection for large temperature gradients around a square solid body within a rectangular cavity. *International Journal of Heat and Mass Transfer*, 50 (17–18):3599–3615, 2007. doi: 10.1016/j.ijheatmasstransfer.2006.05.013.

[56] X. Wen, L.-P. Wang, and Z. Guo. Development of unsteady natural convection in a square cavity under large temperature difference. *Physics of Fluids*, 33(8), 2021. doi: 10.1063/5.0058399.

[57] Y. Huang and H. H. Bau. Thermoacoustic waves in a confined medium. *International Journal of Heat and Mass Transfer*, 40(2):407–419, 1997. doi: 10.1016/0017-9310(96)00068-3.

[58] B. Farouk, E. S. Oran, and T. Fusegi. Numerical study of thermoacoustic waves in an enclosure. *Physics of Fluids*, 12(5):1052–1061, 2000. doi: 10.1063/1.870360.

[59] Y. Miura, S. Yoshihara, M. Ohnishi, K. Honda, M. Matsumoto, J. Kawai, M. Ishikawa, H. Kobayashi, and A. Onuki. High-speed observation of the piston effect near the gas-liquid critical point. *Physical Review E*, 74(1), 2006. doi: 10.1103/physreve.74.010101.

[60] P. Zhang and B. Shen. Thermoacoustic wave propagation and reflection near the liquid-gas critical point. *Physical Review E*, 79(6), 2009. doi: 10.1103/physreve.79.060103.

[61] P. Carlès. Thermoacoustic waves near the liquid-vapor critical point. *Physics of Fluids*, 18(12), 2006. doi: 10.1063/1.2397577.

[62] E. W. Lemmon, I. H. Bell, M. L. Huber, and M. O. McLinden. NIST Standard Reference Database 23: Reference Fluid Thermodynamic and Transport Properties-REFPROP, Version 10. , National Institute of Standards and Technology, 2018. URL https://www.nist.gov/srd/refprop.

[63] S. Amiroudine, P. Bontoux, P. Larroudé, B. Gilly, and B. Zappoli. Direct numerical simulation of instabilities in a two-dimensional near-critical fluid layer heated from below. *Journal of Fluid Mechanics*, 442:119–140, 2001. doi: 10.1017/s0022112001004967.

[64] G. Accary, P. Bontoux, and B. Zappoli. Turbulent Rayleigh–Bénard convection in a near-critical fluid by three-dimensional direct numerical simulation. *Journal of Fluid Mechanics*, 619:127–145, 2009. doi: 10.1017/s0022112008004175.

[65] B. Shen and P. Zhang. Rayleigh–Bénard convection in a supercritical fluid along its critical isochore in a shallow cavity. *International Journal of Heat and Mass Transfer*, 55(23-24):7151–7165, 2012. doi: 10.1016/j.ijheatmasstransfer.2012.07.031.

[66] A.D. Demou and D. G. E. Grigoriadis. Direct numerical simulations of Rayleigh–Bénard convection in water with non-oberbeck–boussinesq effects. *Journal of Fluid Mechanics*, 881:1073–1096, 2019. doi: 10.1017/jfm.2019.787.

[67] J. H. Bae, J. Y. Yoo, and D. M. McEligot. Direct numerical simulation of heated CO2 flows at supercritical pressure in a vertical annulus at Re=8900. *Physics of Fluids*, 20(5), 2008. doi: 10.1063/1.2927488. URL https://doi.org/10.1063/1.2927488.

[68] A.D. Demou, C. Frantzis, and D.G.E. Grigoriadis. A low-mach methodology for efficient direct numerical simulations of variable property thermally driven flows. *International Journal of Heat and Mass Transfer*, 132:539–549, 2019. doi: 10.1016/j.ijheatmasstransfer.2018.12.018.

[69] D. T. Banuti, M. Raju, and M. Ihme. Similarity law for widom lines and coexistence lines. *Physical Review E*, 95(5), 2017. doi: 10.1103/physreve.95.052120.

[70] D. T. Banuti. A critical assessment of adaptive tabulation for fluid properties using neural networks. In *AIAA Scitech 2021 Forum*. American Institute of Aeronautics and Astronautics, 2021. doi: 10.2514/6.2021-0927.

[71] E. Rinaldi, R. Pecnik, and P. Colonna. Exact jacobians for implicit navierstokes simulations of equilibrium real gas flows. *Journal of Computational Physics*, 270:459–477, 2014. doi: https://doi.org/10.1016/j.jcp.2014.03.058. URL https://www.sciencedirect.com/science/article/pii/S0021999114002459.

[72] S. Kawai, H. Terashima, and H. Negishi. A robust and accurate numerical method for transcritical turbulent flows at supercritical pressure with an arbitrary equation of state. *Journal of Computational Physics*, 300:116–135, 2015. doi: https://doi.org/10.1016/j.jcp.2015.07.047. URL https://www.sciencedirect.com/science/article/pii/S0021999115004921.

[73] O. Shishkina, R. J. A. M. Stevens, S. Grossmann, and D. Lohse. Boundary layer structure in turbulent thermal convection and its consequences for the required numerical resolution. *New Journal of Physics*, 12(7):075022, 2010. doi: 10.1088/1367-2630/12/7/075022.

[74] A. Poux, S. Glockner, and M. Azaïez. Improvements on open and traction boundary conditions for Navier–Stokes time-splitting methods. *Journal of Computational Physics*, 230(10):4011–4027, 2011. doi: 10.1016/j.jcp.2011.02.024. URL https://doi.org/10.1016/j.jcp.2011.02.024.

[75] C. Bozonnet, O. Desjardins, and G. Balarac. Traction open boundary condition for incompressible, turbulent, single- or multi-phase flows, and surface wave simulations. *Journal of Computational Physics*, 443:110528, 2021. doi: https://doi.org/10.1016/j.jcp.2021.110528. URL https://www.sciencedirect.com/science/article/pii/S002199912100423X.

[76] M.S. Dodd and A. Ferrante. A fast pressure-correction method for incompressible two-fluid flows. *Journal of Computational Physics*, 273:416–434, 2014. doi: https://doi.org/10.1016/j.jcp.2014.05.024. URL https://www.sciencedirect.com/science/article/pii/S0021999114003702.